Acta Pharmaceutica Sinica B 2024;14(6):2698−2715

Chinese Pharmaceutical Association
Institute of Materia Medica, Chinese Academy of Medical Sciences

Acta Pharmaceutica Sinica B

www.elsevier.com/locate/apsb
www.sciencedirect.com

ORIGINAL ARTICLE

Repurposing disulfiram with CuET nanocrystals: Enhancing anti-pyroptotic effect through NLRP3 inflammasome inhibition for treating inflammatory bowel diseases

Xueming Xu[a,†], Yuanfeng Han[a,b,†], Jiali Deng[a,b,c,†], Shengfeng Wang[d], Shijie Zhuo[b], Kai Zhao[a,*], Wenhu Zhou[b,e,*]

[a]*Hematology and Department of Critical Care Medicine, The Third Xiangya Hospital, Central South University, Changsha 410013, China*
[b]*Xiangya School of Pharmaceutical Sciences, Central South University, Changsha 410013, China*
[c]*Hunan Chidren's Hospital, Changsha 410007, China*
[d]*Department of Pharmacy, The Third Xiangya Hospital, Central South University, Changsha 410013, China*
[e]*Key Laboratory of Biological Nanotechnology of National Health Commission, Changsha 410008, China*

Received 15 November 2023; received in revised form 4 January 2024; accepted 29 January 2024

KEY WORDS

Drug repurposing;
Pyroptosis;
Nanoparticles;
Bioavailability;
Disulfiram;
DSS-induced colitis;
NLRP3 inflammasome;
CuET

Abstract Drug repurposing offers a valuable strategy for identifying new therapeutic applications for existing drugs. Recently, disulfiram (DSF), a drug primarily used for alcohol addiction treatment, has emerged as a potential treatment for inflammatory diseases by inhibiting pyroptosis, a form of programmed cell death. The therapeutic activity of DSF can be further enhanced by the presence of Cu^{2+}, although the underlying mechanism of this enhancement remains unclear. In this study, we investigated the mechanistic basis of Cu^{2+}-induced enhancement and discovered that it is attributed to the formation of a novel copper ethylthiocarbamate (CuET) complex. CuET exhibited significantly stronger anti-pyroptotic activity compared to DSF and employed a distinct mechanism of action. However, despite its potent activity, CuET suffered from poor solubility and limited permeability, as revealed by our druggability studies. To overcome these intrinsic limitations, we developed a scalable method to prepare CuET nanocrystals (CuET NCs) using a metal coordination-driven self-assembly approach. Pharmacokinetic studies demonstrated that CuET NCs exhibited a 6-fold improvement in bioavailability. Notably, CuET NCs exhibited high biodistribution in the intestine, suggesting their potential application for the treatment

*Corresponding authors.
E-mail addresses: kaizhao@csu.edu.cn (Kai Zhao), zhouwenhuyaoji@163.com (Wenhu Zhou).
†These authors made equal contributions to this work.
Peer review under the responsibility of Chinese Pharmaceutical Association and Institute of Materia Medica, Chinese Academy of Medical Sciences.

https://doi.org/10.1016/j.apsb.2024.03.003

of inflammatory bowel diseases (IBDs). To evaluate their therapeutic efficacy *in vivo*, we employed a murine model of DSS-induced colitis and observed that CuET NCs effectively attenuated inflammation and ameliorated colitis symptoms. Our findings highlight the discovery of CuET as a potent anti-pyroptotic agent, and the development of CuET NCs represents a novel approach to enhance the druggability of CuET.

1. Introduction

The development of new drugs is a time-consuming and expensive process. However, drug repurposing, also known as "new uses for old drugs", provides a promising strategy for expedited drug development by repurposing existing drugs for different therapeutic applications[1,2]. Disulfiram (DSF) is an oral aldehyde dehydrogenase (ALDH) inhibitor that has been approved by the US Food and Drug Administration for the treatment of alcoholism, with a long history of clinical use[3-5]. In recent years, DSF has garnered attention as a potential anticancer drug through drug repurposing, particularly in combination with Cu^{2+} [6–9]. The combination of DSF and copper (DSF/Cu) has demonstrated remarkable anticancer activity, effectively inhibiting tumor proliferation, metastasis, and targeting cancer stem cells[10]. Clinical trials have been initiated to evaluate its efficacy in treating various types of tumors, such as glioblastoma and multiple myeloma[11]. Several mechanisms have been proposed to explain the anticancer activity of DSF/Cu^{2+} combination therapy[12–18]. Notably, a groundbreaking study has highlighted the crucial role of *in vivo* metabolism of DSF into diethyldithiocarbamate (DTC) in enhancing its anticancer properties[17]. DTC forms a metal complex with copper, referred to as CuET, which exhibits potent anticancer effects. CuET acts by targeting the interaction between p97 and the proteasome substrate adaptor, nuclear protein localization-4 (NPL4), leading to the inhibition of substrate degradation and induction of cancer cell death. These findings position CuET as a promising candidate for targeted drug repurposing, showcasing its significant potential in utilizing DSF for novel therapeutic applications.

Recently, DSF has been reported to exhibit anti-pyroptosis effect[19–21]. Pyroptosis is a type of inflammatory cell death mediated by the gasdermin protein family[22–24]. It is triggered by inflammasomes, which are supramolecular complexes that recruit and activate inflammatory caspases to cleave gasdermins. Among them, gasdermin D (GSDMD) is the first reported executor of pyroptosis[25,26]. Upon cleavage at Asp275 (mouse Asp276) in the linker region, the N-terminal domain of GSDMD (GSDMD-NT) oligomerizes and forms pores with a diameter of 10−20 nm on cellular membranes. This leads to the release of intracellular inflammatory mediators, including IL-1β. Previous research has suggested that DSF inhibits the NF-κB-dependent pathway, thereby suppressing tumor cell proliferation and differentiation, indicating its anti-inflammatory potential[27]. However, recent work by Hao Wu's group[19] has shed light on the more detailed anti-inflammatory effects of DSF. They demonstrated that DSF inhibits NLRP3 inflammasome- and non-canonical inflammasome-induced pyroptosis, along with the secretion of associated inflammatory cytokines. Furthermore, DSF was found to alleviate sepsis in a mouse model. Mechanistically, DSF covalently modifies human/mouse Cys191/Cys192 in GSDMD, thereby blocking its pore formation. Due to its anti-inflammatory properties, DSF has been widely explored in the treatment of various inflammatory diseases, including sepsis[19], COVID-19 infection[20], steatohepatitis[28], type II diabetes[29], angiogenesis[15], osteoarthritis[30], and inflammatory bowel diseases (IBD)[31]. Interestingly, researchers have observed that Cu^{2+} enhances the anti-pyroptotic effects of DSF both *in vitro* and *in vivo*[19]. However, the detailed mechanism is still elusive.

Drawing upon the synergistic effect of Cu^{2+} on DSF in tumor therapy, we hypothesized that the enhanced anti-pyroptotic effect of DSF by Cu^{2+} might also be attributed to the formation of CuET. In this study, we initially confirmed the augmented anti-pyroptotic effect of DSF in the presence of Cu^{2+} using a cell proptosis model. Subsequently, we demonstrated that this enhancement was indeed a result of the *in situ* generation of CuET within cells. This finding positions CuET as a promising candidate for the development of anti-pyroptosis drugs, motivating us to further explore its fundamental druggability properties.

Regrettably, CuET exhibited poor solubility in both aqueous and organic solvents and displayed limited permeability in a Caco-2 cell monolayer model, classifying it as a type IV drug candidate according to the biopharmaceutical classification system (BCS). To overcome these challenges, we devised a scalable method for producing CuET nanocrystals (CuET NCs) to facilitate biomedical applications (Scheme 1)[32,33]. This approach involved a facile metal coordination-mediated self-assembly technique. Subsequently, we employed CuET NCs to unravel the intricate mechanism underlying its anti-pyroptotic effects. Our findings revealed that CuET operated through a distinct mechanism compared to DSF by impeding inflammasome assembly—an upstream event of pyroptosis—resulting in the specific inhibition of NLRP3 inflammasome activation. Specifically, our results suggested that CuET exerted its inhibitory effect on NLRP3 inflammasome assembly by interfering with the interaction between NLRP3 and NEK7, thereby disrupting ASC speck formation and effectively inhibiting NLRP3 inflammasome-mediated pyroptosis. Furthermore, we conducted a pharmacokinetic study to evaluate the advantages of the nanocrystal formulation, which revealed a remarkable 6-fold increase in relative bioavailability compared to CuET suspension (CuET SP) after oral administration at a dose of 60 mg/kg. Intriguingly, biodistribution analysis indicated significant accumulation of CuET in the intestine, indicating its potential application in the treatment of inflammatory diseases affecting the digestive system. Based on these observations, we assessed CuET NCs in a murine model of DSS-induced colitis, where we achieved satisfactory efficacy as evidenced by clinical parameters and pathological analyses. This study identified CuET as a potent anti-

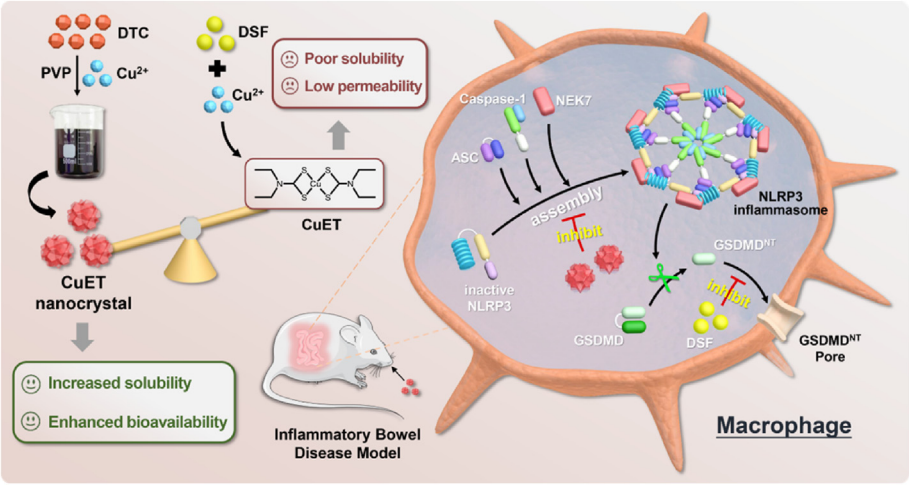

Scheme 1 Illustration the mass production of CuET NCs to solve the key limitations of CuET druggability for IBD therapy, and the anti-pyroptotic mechanism of CuET through NLRP3 inflammasome inhibition.

pyroptotic agent, characterized its fundamental druggability properties, and developed a scalable nanocrystal formulation to overcome the limitations of poor solubility and permeability. The discovery of CuET's specific inhibitory effect on NLRP3 inflammasome assembly, accomplished by disrupting the NLRP3-NEK7 interaction, not only advances our understanding of inflammasome regulation but also offers promising therapeutic avenues for inflammatory diseases.

2. Materials and methods

2.1. Materials

Ultrapure Lipopolysaccharide (LPS, *E. coli* 0111: B4, Cat No. tlrl-3pelps), Standard LPS (*E. coli* 0111: B4, Cat No. tlrl-eblps), ATP (Cat No. tlrl-atpl), nigericin (Cat No. tlrl-nig), MSU (Cat No. tlrl-msu), Flagellin, Poly(da:dT) were purchased from InvivoGen (San Diego, CA, USA). Lipofectamine 3000 transfection reagent (Cat No. L3000015) is from Thermo Fisher (Waltham, MA, USA), Mouse immunoglobin IgG protein (Cat No. ab198772) was purchased from abcam (Cambridge, UK). Protein A/G PLUS-Agarose (Cat No. sc-2003) came from Santa Cruz (Dallas, Texas, USA), Cell lysis buffer (CLB, Cat No. 9803) was purchased from Cell Signaling Technology (Danvers, MA, USA). Mouse IL-1β (Cat No. 88-7013) and Human IL-1β (Cat No. BMS22) Elisa Kit were purchased from Thermo Fisher (Waltham, MA, USA).

Diethyldithiocarbamate (DTC, 228,680) and disulfiram (DSF) were purchased from Sigma−Aldrich (St. Louis, MO, USA). Copper chloride dehydrate ($CuCl_2 \cdot 2H_2O$) was obtained from Macklin (Shanghai, China). Polyvinylpyrrolidone K30 (PVP, 30,154,482) and sodium carboxymethyl cellulose (CMC-Na, 30,036,328) were purchased from Sinopharm (Beijing, China). RPMI-1640 medium and fetal bovine serum (FBS) were obtained from Gibco (Carlsbad, CA, USA). Phosphate buffered saline (PBS, P1022), penicillin-streptomycin solution (P1410), 0.25% (*w*/*v*) trypsin solution (T1300), thiazolyl blue (MTT, M8180) and 4′,6-diamidino-2-phenylindole (DAPI, C0065) were provided by Solarbio (Beijing, China). Copper (II) diethyldithiocarbamate (CuET, >97%, C154088) and bovine serum albumin (BSA, ≥98%, B265993) were purchased from Aladdin (Shanghai, Beijing). Rat plasma (ZRP231) was purchased from Beijing Zhengbo Weiye Biotechnology Co., Ltd. Acetonitrile, and formic acid (FA, 1.00263) were provided by Merck & Co., Inc. (Kenilworth, USA), and other reagents were provided by China national pharmaceutical group corporation chemical reagent Co., Ltd. Anti-IL-1β (1:1000, *v*/*v*, AF-401-NA) was purchased from RD system (Abingdon, UK), Anti-NLRP3 (1:1000, *v*/*v*, AG-20B-0014), ASC (1:1000, *v*/*v*, AG-25B-0006) were purchased from Adipogen (San Diego, CA, USA), anti-Caspase-1 (1/1000, *v*/*v*, ab179515), anti-NEK7 (1:5000, *v*/*v*, ab133514), anti-GSDMD (1/1000, *v*/*v*, ab209845) were purchased from Abcam; anti-β-actin (1/10,000, *v*/*v*, BH10D10) was purchased from Cell Signaling Technology (Danvers, MA, USA), DyLight 488-labeled secondary antibody (1:50, A120-100D2) were purchased from InvivoGen (San Diego, CA, USA).

2.2. Cells

Primary peritoneal macrophages from 6-8-week-old C57BL/6 mice were elicited using intraperitoneal injection of 3% thioglycolate broth. After 72 h, cells were collected by peritoneal lavage with 10−15 mL of RPMI-1640 (Gibco, Grand Island, NY, USA). The cells were cultured in RPMI-1640 with 10% FBS, 100 U/mL penicillin and 100 μg/mL streptomycin at 37 °C in 5% CO_2. Caco-2 cells (Procell, Wuhan, China) were cultured in MEM with 1% non-essential amino acid, 20% FBS, 100 U/mL penicillin and 100 μg/mL streptomycin at the same conditions.

2.3. Animals

Wild-type (WT) C57BL/6 male mice (6-10-week-old) and SD rats (160−210 g) from Hunan SJA Laboratory Animal Co., Ltd. (Changsha, China), and they were bred under SPF conditions. All the experimental procedures had been conducted following a protocol approved by the Institutional Animal Care and Use Committee of Xiangya School of Pharmaceutical Sciences, Central South University (202230601).

2.4. HPLC-MS analysis of intracellular CuET

Determination of CuET was performed on a high-performance liquid chromatography-mass spectrometry (HPLC-MS) system (Agilent, Stuttgart, Germany) consisting of a 1290 Infinity II system and a 6470 LC/TQ mass spectrometer. Chromatographic separation was utilized an Agilent Eclipse Plus C18 RRHD column (2.1 mm × 50 mm, 1.8 μm) at 30 °C. Mobile phase: 70% acetonitrile, 30% water, and 0.1% FA. Injection volume: 1.0 μL, flow rate: 0.4 mL/min. Electrospray ionization mass spectrometer operated in positive ion mode with capillary voltage of 4000 V, drying gas flow of 6 L/min, and temperature of 300 °C. CuET quantification performed by single ion monitoring (SIM) mode, detecting fragmentation *m/z* of 359.

2.5. Sample preparation for HPLC−MS analysis

Primary peritoneal macrophages were added to 25 mL culture flasks at a density of 3×10^6 cells per flask. After the cells were attached, different concentrations of DSF (2, 10 and 30 μmol/L) or DSF + $CuCl_2$ combination (C_{DSF} = 2 μmol/L, C_{CuCl_2} = 0, 0.2, 0.4, 1 and 2 μmol/L) were added. After 1 h of incubation, the mediums were replaced with fresh medium, and the cells were cultured for additional 3 h. Then, the medium was removed, and cell lysates were obtained by using freeze-thaw and ultrasonication method as follows. Macrophages were scraped and collected in centrifuge tubes. After washing twice with PBS and resuspending in double-distilled water, the cells were frozen in liquid nitrogen, melted at room temperature, and then repeated freezing and thawing for three times. Next, the cells were sonicated 40 w for 60 s. The cell lysate was then mixed with four times the volume of methanol and centrifuged 15,000 rpm for 15 min (TGL20M, Yingtai, Changsha, China), and supernatant was collected for CuET measurement. To enable an approximate quantification of intracellular CuET, various standard solutions of CuET were spiked in blank cytoplasm and then mimicked sample processing to plot a standard curve.

2.6. Preparation and yield of CuET NCs

According to the previous research results[34], a fixed ratio (2/1, *mol/mol*) between DTC and Cu^{2+} was used. Ultra-pure water served as the solvent, while PVP (*w/w*) was added as a stabilizer at a final concentration ranging from 0.4% to 2%. $CuCl_2$ solution was loaded into a syringe and connected to a constant flow pump, ensuring a drip rate below 5 mL/h. At room temperature, three separate groups of CuET NCs were prepared, each with different mass concentrations.

CuET NCs were lysed with acetonitrile, followed by HPLC−MS/MS analysis for quantitative determination. To enable an adequate quantification of analyzed CuET, a calibration curve was prepared. Yield was calculated as the ratio of actual concentration to theoretical concentration.

2.7. Preparation of CuET suspension (CuET SP)

Appropriate amount of CuET powders was weighed precisely and added into CMC-Na aqueous solution, ultrasonically dispersed, and the final concentration of CMC-Na in the whole system was 0.5% (*w/v*), which was obtained as CuET SP.

2.8. Characterization of CuET NCs

The average size and ζ potential of CuET NCs were detected by Malvern Zeta Sizer Nano series (ZS-90, Malvern Instruments, Great Malvern, UK). The morphology of CuET NCs was observed using transmission electron microscopy (Titan G2 60-300, FEI, Hillsboro, USA). A UV−Vis absorption spectrometer (UV-2600i, Shimadzu, Japan) and Fourier transform infrared (FTIR) spectrometer (AVATAR360, Nicolet, Wisconsin, USA) were used to study the chemical structure of CuET NCs. Powder X-ray diffraction (XRD) patterns of CuET NCs was acquired on an X-ray diffractometer (Empyrean 2, PANalytical, Holland).

2.9. Cytotoxicity assay

Primary peritoneal macrophages were plated in 96-well plates at a density of 3.5×10^4 cells per well and incubated at 37 °C with 5% CO_2 for 22 h. Cells were then treated with new culture mediums containing different concentrations of CuET NCs. After 1 h of incubation, the mediums were replaced with fresh medium, and the cells were cultured for additional 18 h. Then, 0.5 mg/mL MTT solution were added to each well and the cells were cultured for an another 4 h. Next, the supernatant was removed, and dimethyl sulfoxide (DMSO) was used to dissolve formazan crystals before the optical density (OD) assay at 570 nm. The cell viability was computed as the percentage of the OD value of sample *versus* that of control (Supporting Information Fig. S1).

2.10. HPLC-UV analysis of CuET

HPLC evaluations were conducted using an Agilent 1260 Infinity II HPLC system with a VMD detector. A C-18 reverse phase column (4.6 mm × 150 mm, 5 μm) from Agilent Technologies Inc. was utilized, maintained at a constant temperature of 30 °C. The mobile phase consisted of 0.1% (*v/v*) FA in water (A) and 100% acetonitrile (B), with an isocratic flow rate of 1 mL/min. Detection was performed at 433 nm, and each analysis involved injecting 20 μL of the sample.

2.11. Sample preparation for equilibrium solubility

Excess CuET was weighed and transferred to stopper glass test tubes. Ultrapure water, PBS (10 mmol/L, pH 4.0−9.0), methanol, ethanol, and other organic solvents were individually added. After 10 min of sonication and mechanical oscillation at 37 °C and 100 rpm, the saturated solution was collected after 12 and 48 h. Centrifugation at 12,000 rpm (TGL18, Yingtai Instrument Co., Ltd., Changsha, China) and 25 °C for 10 min was performed, and the supernatant was diluted with acetonitrile for HPLC−UV analysis. To enable an adequate quantification of analyzed CuET, a calibration curve was prepared.

2.12. Transport of CuET across Caco-2 cell monolayer

The permeability of CuET across the Caco-2 cell monolayers was investigated from the apical (0.5 mL) to basolateral direction (1.5 mL) in D-HBSS buffer solution with 0.001% Tween 80 (pH 7.4). After seeding 500 μL of cells at the concentration of 2×10^5 cells/mL in 12-well cell culture inserts (3460 Transwell, Corning, NY, USA), the medium was replaced every other day until the cell monolayer was formed after 18−21 days. TEER values monitored monolayer integrity using EVOM2 (World

Precision Instruments LLC, FL, USA). For the permeability experiments (AP to BL), 0.5 mL of 1, 5, 10 μg/mL CuET was added to the apical chamber, and the plates were shaken at 100 rpm at 37 °C. 200 μL of samples were withdrawn from the basolateral chamber at different time points (30, 60, 90, 120 and 150 min), and the same volume of fresh buffer solution was added to replace the withdrawn volume. The concentration of CuET was determined by HPLC-MS/MS analysis. Each experiment was performed in triplicate. The apparent permeability coefficient (P_{app}) and efflux ratio (ER) were calculated as described elsewhere[35,36].

2.13. Assay stability of CuET in plasma or BSA

CuET was dissolved in acetonitrile, then mixed with rat plasma or BSA solution (50 mg/mL) and vortexed with acetonitrile (CuET/plasma or BSA/ACN = 1/19/80, *v/v/v*). HPLC-MS/MS was utilized for determination of CuET, and the peak area was recorded as A_0. After storage at room temperature for 0, 2, 4, 8, 12 and 24 h, detected CuET was calculated according to Eq. (1):

$$\text{Detected CuET}\ (\%) = |\frac{A_T}{A_0} - 1| \times 100 \quad (1)$$

where A_T is the CuET content at the time of testing, A_0 is the initial CuET content.

2.14. Binding mechanism analysis

Fluorescence spectra were determined by HITACHI F-2700 fluorescence spectrometer with an excitation wavelength 280 nm. The spectral bandwidths were 10 and 2.5 nm for excitation and emission, respectively. The fluorescence spectra of BSA were recorded in the wavelength range of 280−450 nm. The BSA samples were titrated with increasing concentrations of CuET solution (ethanol as solvent, titrate no more than 30 μL). The slit widths, excitation voltage, and scan speed were kept constant within each data set. All samples were measured in a quartz cuvette (path length 1 cm). Titrations were performed manually using a micropipette. For each titration, the fluorescence emission spectrum of BSA in the reaction solution was collected with BSA at the concentration of 1.0 μmol/L (in PBS buffer, pH 7.4). The fluorescence quenching effects and the binding interaction between CuET and BSA can be described by the Stern−Volmer equation and Double logarithmic regression equation[37,38].

2.15. HPLC-MS/MS analysis of CuET

Cell transport samples were analyzed using an HPLC-MS/MS system (Agilent, Stuttgart, Germany) consisting of a 1290 Infinity II system and a 6470 LC/TQ mass spectrometer. Positive ion mode with AJS ESI source was used, operating at standard parameters. Chromatographic separation utilized a YMC-Triart C18 column (50 mm × 2.1 mm, 3 μm; Japan) at 35 °C with a flow rate of 600 μL/min. The mobile phase was 0.1% FA in water (A) and 100% acetonitrile (B). Mass spectra were analyzed with Agilent MassHunter quantitative software. Extracted ion chromatograms of transitions 116.0 were smoothened with width of two points for CuET analysis. Plasma and tissue samples were analyzed using a UPLC-MS/MS system consisting of a Nexera UHPLC/HPLC system (Shimadzu Corp., Kyoto, Japan) coupled with a Hybrid API 5500 QTrap mass spectrometer. Positive ion mode with DuoSpray ESI source was employed, Chromatographic separation was performed using a Gemini C6-Phenyl 110ALC column (50 mm × 3 mm, 3 μm; Phenomenex, USA) at 40 °C and a flow rate of 600 μL/min with isocratic chromatography. The mobile phase and acquisition parameters were as previously described. Data acquisition, peak integration, and calculation were done using Analyst™ software. Extracted ion chromatograms of transitions 116.0 were appropriately smoothed, and peak area was recorded. To ensure accurate quantification, content determination methodology was carefully prepared, as illustrated in Supporting Information Figs. S2, S3, and Tables S1−S4.

2.16. Sample preparation for HPLC−MS/MS analysis

In the CuET absorption mechanism study, the blank cell transport solution was D-HBSS containing 0.001% Tween 80. After cell transport, CuET was extracted in a 1:19 (*v/v*) ratio of transport solution to 100% acetonitrile, filtered using a 0.22 μm organic filter membrane, and analyzed within 6 h. In the concentration−time curve study, SD rats were divided into two groups and orally administered either CuET SP or CuET NCs at a dose of 60 mg/kg. Blank blood was collected before administration, and blood was collected at specified time points (0.083, 0.25, 0.5, 1, 2, 4, 6, 8, 12, and 24 h) thereafter. Approximately 0.5 mL of blood was collected each time, immediately put into pre-cooled tubes containing sodium heparin as an anticoagulant and cooled on ice. The collected blood samples were immediately centrifuged at 4000 rpm (TGL18, Yingtai Instrument Co., Ltd.) for 10 min at 4 °C. Plasma was collected, mixed with three times the volume of ice-cold acetonitrile, vortexed, and then centrifuged at 12,000 rpm for 5 min at −20 °C. The supernatant was filtered through a 0.22 μm organic membrane, transferred to a pre-cooled 96-well deep-well plate, sealed, and immediately analyzed using a pre-cooled (4 °C) LC sample holder.

In the tissue distribution study, SD rats were euthanized, and tissue samples were collected within 5 min. The samples were washed with saline, and the gastrointestinal tissue was rinsed. Surface water was removed, and samples were snap-frozen in liquid nitrogen promptly. The entire sampling process took 15 min. Frozen samples were homogenized in ice-cold acetone (1:10, *v/v*) using a table-top homogenizer with glass balls (JXFSTPRP-48L, Shanghai Jinxin, China) for 1 min at 60 Hz. After centrifugation at −20 °C, 12000 rpm (TGL18, Yingtai Instrument Co., Ltd.) for 5 min, the supernatant was transferred to a pre-cooled 96-well deep-well plate, sealed, and immediately placed in a pre-cooled (4 °C) LC sample holder for analysis. All biological samples were promptly processed and analyzed after collection. Ice-cold acetonitrile (−20 °C) and ice-cold acetone (pre-cooled in dry ice) were used. Grinding molds and tubes were also pre-cooled in dry ice.

2.17. CD measurements

The BSA's secondary structure changes were analyzed using a J-815CD spectrometer (Jasco, Japan) in the far-UV region (260−200 nm). CD spectra were recorded at 200 nm/min, 0.5 nm pitch, and 1.00 nm width. PB buffer solution (pH 7.4, 0.1 mol/L) was prepared with potassium dihydrogen phosphate and dipotassium hydrogen phosphate. BSA (5 μmol/L) was dissolved in the PB buffer and placed in a 1 cm quartz cell. Each sample was scanned three times, and CD spectra were baseline-corrected by subtracting the PB buffer spectra.

2.18. Macrophages inflammasome activation

Macrophages were plated in 24-well plates at 3×10^5–4×10^5 cells per well overnight. Mice macrophages were primed with 100 ng/mL ultrapure LPS for 3 h, then followed by stimulation with 10 μmol/L nigericin (1 h), 5 mmol/L ATP (1 h), 200 μg/mL MSU (6 h), 1 μg/mL poly(da:dT, 16 h) and 2 μg/mL flagellin (1 h). For non-canonical inflammasome activation, macrophages were primed with 100 ng/mL ultrapure LPS for 3 h, then transfected with 2 μg/mL ultrapure LPS for 16 h. After stimulation, all the supernatants or cell lysates were collected for immunoblotting analysis and the cell supernatants were used for LDH assay and ELISA analysis.

2.19. THP-1 cell culture and stimulation

THP-1 cells were cultivated in RPMI with 10% FBS, 100 U/mL penicillin and 100 μg/mL streptomycin at 37 °C and 5% CO_2. At the progress of experiment, THP-1 cells were differentiated by 100 ng/mL PMA (Invivogen 6414-43-02, San Diego, CA, USA) overnight. THP-1 cells were primed with 1 μg/mL ultrapure LPS for 6 h, then followed by stimulation with 10 μmol/L nigericin (2 h), 5 mmol/L ATP (2 h), 200 μg/mL MSU (6 h), 1 μg/mL poly da:dT (16 h) and 2 μg/mL flagellin (2 h). For non-canonical inflammasome activation, macrophages were primed with 1 μg/mL ultrapure LPS for 6 h, then transfected with 2 μg/mL ultrapure LPS for 16 h. The cell supernatants were used for LDH assay and ELISA analysis.

2.20. ASC speck formation and oligomerization assay

Macrophages were seeded on chamber slides overnight and then stimulated with indicated inflammasome stimuli. After stimulation, the cells were washed three times with PBS buffer, fixed in 4% Paraformaldehyde (PFA) for 10 min, permeabilized with 0.1% Triton X-100 for 15 min, and blocked with PBS buffer containing 3% BSA. Cells were stained with anti-ASC antibody (1:200, *v*/*v*) at 4 °C for 12 h and DyLight 488-labeled secondary antibody (1:50, *v*/*v*) at room temperature for 1 h. Lastly, DAPI was used to stain nuclei. Cells were visualized by fluorescence microscope (Nikon Ti2−U).

For ASC oligomerization, primary peritoneal macrophage cells were lysed with Triton buffer (50 mmol/L Tris−HCl pH 7.5, 150 mmol/L NaCl, 0.5% Triton-X100) and 0.1 mmol/L phenylmethylsulfonylfluoride (PMSF) for 10 min at 4 °C. The cell lysates were centrifuged at 6000×*g* (Eppendorf, 5424R, Hamburg, Germany) for 15 min at 4 °C. Supernatants were transferred to new tubes as Triton-soluble fractions. The Triton-insoluble pellets were washed twice with TBS buffer and then suspended in 200 mL TBS. The resuspended pellets were then cross-linked at room temperature for 30 min with 2 mmol/L disuccinimidyl suberate (TCI, D3895, Shanghai, China) and then were centrifuged for 15 min at 6000×*g*. The pellets were dissolved in sodium dodecyl sulphate (SDS) sample buffer.

2.21. Immunoprecipitation and Western blot

After stimulation peritoneal macrophages were lysed in immunoprecipitation (IP) buffer containing 50 mmol/L Tris HCl (pH 7.4), 50 mmol/L EDTA, 200 mmol/L NaCl, and 1% NP-40. supplemented with a protease inhibitor cocktail, pre-cleared cell lysates were then subjected to specific antibodies overnight and protein G plus-agarose for 2 h, then washed four times with IP buffer. The immunoprecipitation complex was dissolved in SDS loading buffer for Western blotting.

For immunoblot analysis, cells were lysed with CLB supplemented with protease inhibitor cocktail and PMSF, and then the cell lysates were centrifugated at 12,000×*g* (Eppendorf 5424R) for 5 min at 4 °C. Equal amounts of extracts were separated by SDS-PAGE, and then they were transferred onto 0.22 mm PVDF membranes (Merck Millipore, ISEQ00010, Billerica, MA, USA) for immunoblot analysis.

2.22. Hemolysis test

Fresh blood samples were collected from healthy mice. The red blood cells (RBCs) were isolated by centrifugation followed by washing with PBS for three times. Next, saline was added to prepare 2% RBCs. CuET NCs, deionized water and saline were mixed with same volume of 2% RBCs and then incubated at 37 °C for 3 h followed by centrifugation at 1500 rpm for 15 min. The absorbance of sample supernatants at 576 nm was measured to calculate the hemolysis rate.

2.23. LPS-induced acute systemic inflammation

C57BL/6 mice were pretreated with or without CuET NCs 4 h earlier, then injected intraperitoneally with 20 mg/kg LPS. After 8 h, mice were sacrificed to collect the serum and lung. The serum concentrations of IL-1β and IL-6 were measured by ELISA.

2.24. DSS-induced colitis

For acute experimental colitis induction, C57BL/6 mice were treated with 3% DSS or Saline in their drinking water for 9 days[39,40]. During the experiment, body weights, stool, and body posture were monitored daily to assess DAI. The DAI is the combined score of weight loss compared with initial weight, stool consistency, and bleeding. (a) weight loss (0 point = none, 1 point = 1%−5% weight loss, 2 points = 5%−10% weight loss, 3 points = 10%−15% weight loss and 4 points = more than 15% weight loss), (b) stool consistency or diarrhea (0 points = normal, 2 points = loose stools, 4 points = watery diarrhea), (c) bleeding (0 points = no bleeding, 2, slight bleeding, 4 points, gross bleeding. Mice were euthanized at the indicated time points, and the colon was immediately collected for colon length measurement, colon explant culture, colon Western blot analysis and histological analysis.

2.25. Colonics immunoblot analysis

Mouse intestinal tissues were dissolved in SDS lysate at a certain ratio (1/20, mg/μL). The samples were sonicated and ground, centrifuged at 12,000 ×*g* for 10 min, and Western blotting was performed after protein quantification.

2.26. Histological analysis

The mouse tissue was fixed in 4% PFA at 4 °C for 24 h and sectioned after embedding in paraffin. The sections were prepared and stained with H&E using standard procedures. The slides were inspected under the Nikon ECL IPSE Ci biological microscope, and images were captured with a Nikon DS-U3 color digital camera.

2.27. *Statistical analysis*

Statistical analyses were performed using GraphPad Prism 8.0 and Microsoft Excel 2010 software. All values are expressed as mean ± standard deviation (SD). Two-sample comparisons were analyzed using Student's *t*-test, and one-way analysis of variance was used for multiple comparisons.

3. Results and discussion

3.1. *Enhanced anti-pyroptosis effect of DSF via in situ generation of CuET by Cu^{2+}*

To investigate the anti-pyroptosis activity of DSF, we utilized a cell proptosis model induced by LPS-nigericin. Initially, we evaluated the effectiveness of DSF by measuring LDH levels and IL-1β production in a dose-dependent manner (Fig. 1A and B). Consistent with a previous report[19]. DSF exhibited a dose-dependent inhibition of pyroptosis, with significant activity observed at 5 μmol/L and optimal efficacy at 30 μmol/L.

Next, we explored the impact of Cu^{2+} on DSF efficacy at the cellular level. DSF was held constant at 2 μmol/L (which exhibited no significant activity at this concentration), and various concentrations of Cu^{2+} were added (Fig. 1C and D). Interestingly, the anti-pyroptosis effect was progressively enhanced with higher Cu^{2+} concentrations. The most substantial enhancement occurred at a DSF/Cu^{2+} molar ratio of 1:1, resulting in efficacy comparable to that of 30 μmol/L DSF alone, as evidenced by the suppression of LDH release and IL-1β production. In contrast, free Cu^{2+} alone had no effect on cell pyroptosis (Fig. 1E and F), which is consistent with another study[41]. Consequently, this enhancement is likely due to the combination of Cu^{2+} and DSF. Notably, previous studies have observed a similar Cu^{2+}-induced enhancement of DSF efficacy when repurposing DSF for the treatment of tumors[17]. The mechanism of Cu^{2+} sensitization has been explicitly elucidated as the formation of the metallic compound CuET. In this proposed mechanism, DSF is initially degraded to produce

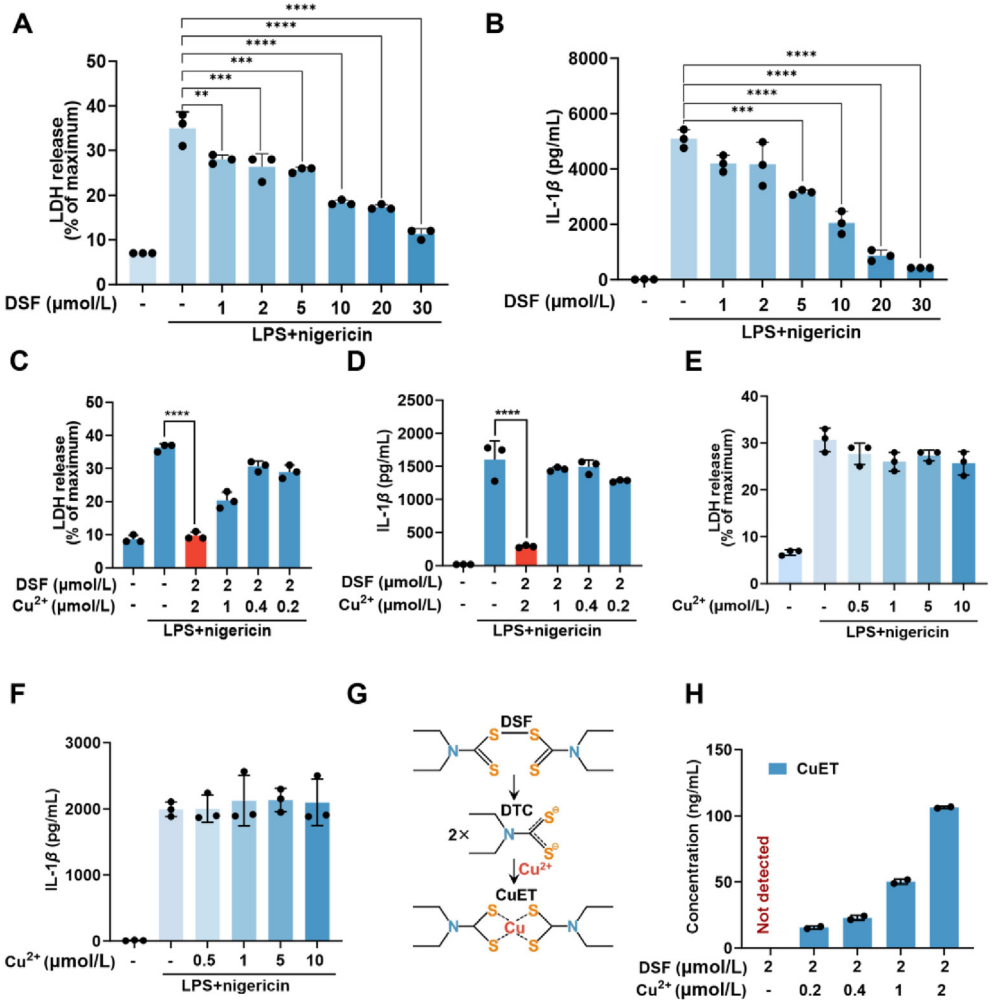

Figure 1 LDH release (A) and IL-1β levels (B) in the supernatant of LPS-primed primary macrophages treated with varying doses of DSF and stimulated with nigericin. LDH release (C) and IL-1β levels (D) in the supernatant of LPS-primed primary macrophages treated with varying doses of $CuCl_2$ and 2 μmol/L DSF, followed by nigericin stimulation. LDH release (E) and IL-1β levels (F) in the supernatant of LPS-primed primary macrophages treated with varying doses of $CuCl_2$ and stimulated with nigericin. (G) Model illustrating CuET formation during the metabolic processing of DSF. (H) Production of CuET detected by LC-MS in cells treated with Cu^{2+}/DSF. Data are presented as mean ± SD ($n = 3$); $^{**}P < 0.01$, $^{***}P < 0.001$, and $^{****}P < 0.00001$, *vs.* indicated.

diethyldithiocarbamate (DTC), which subsequently coordinates with Cu^{2+} to form CuET (Fig. 1G).

Motivated by these findings, we speculated that the enhanced anti-pyroptosis effect of DSF by Cu^{2+} could also be attributed to the *in situ* generation of CuET inside cells. To confirm this hypothesis, cells were treated with the combination of Cu^{2+}/DSF or DSF alone, and CuET generation in cell lysates was detected using LC-MS. Remarkably, CuET generation was observed in the Cu^{2+}/DSF group, and its concentration increased proportionally with higher Cu^{2+} concentrations in the treatment. These results indicate that the mechanism underlying Cu^{2+}-induced DSF enhancement also involves the formation of CuET. In contrast, no CuET generation was detected in the free DSF group, even at concentrations up to 30 μmol/L, suggesting distinct mechanisms of action between DSF and CuET in inhibiting pyroptosis (Supporting Information Fig. S4). Further exploration of these mechanisms will be discussed below.

3.2. *Physiochemical characterization of CuET as drug candidate*

The above studies have highlighted the potential of CuET as an anti-proptosis agent for the treatment of various proptosis-related diseases. However, as a new drug candidate, the physiochemical properties of CuET remain unclear, which could potentially limit its biomedical applications. Therefore, we conducted a comprehensive physiochemical characterization of CuET to assess its suitability as a drug.

Initially, we evaluated the solubility and permeability of CuET, which are fundamental pharmaceutical parameters. Solubility tests were performed in test tubes, revealing that CuET exhibited poor solubility in both water and common organic solvents (Fig. 2A). Following a 48-h equilibration period, the apparent solubility of CuET was quantified in various solutions. Among aqueous solutions, water demonstrated the highest solubility (500 ng/mL), while solubility decreased with increasing pH (Fig. 2C). In organic solvents, the overall solubility was slightly higher. Dimethyl sulfoxide exhibited the highest solubility (around 3.64 mg/mL), followed by acetone, ethyl acetate, and acetonitrile. The solubility in other solvents was below 0.6 mg/mL (Fig. 2D). Consequently, CuET can be classified as an insoluble drug candidate.

Apart from solubility, permeability is another crucial parameter that determines drug bioavailability. To assess this, we developed an *in vitro* Caco-2 cell monolayer model (Fig. 2E). Bidirectional transport studies were conducted to investigate drug uptake (apical to basolateral) and efflux (basolateral to apical). CuET exhibited concentration- and time-dependent transportation profiles at 1, 5, and 10 μg/mL over a period of 2.5 h (Fig. 2F and G), allowing the calculation of apparent permeability (P_{app}) values. Specifically, the P_{app} value (apical to basolateral) was found to be less than 1×10^{-6} (Fig. 2H), indicating poor permeability of CuET. Furthermore, no significant difference was observed in the bidirectional P_{app} values at different CuET concentrations, resulting in ER of approximately 1, suggesting passive transport of CuET in the Caco-2 cell model.

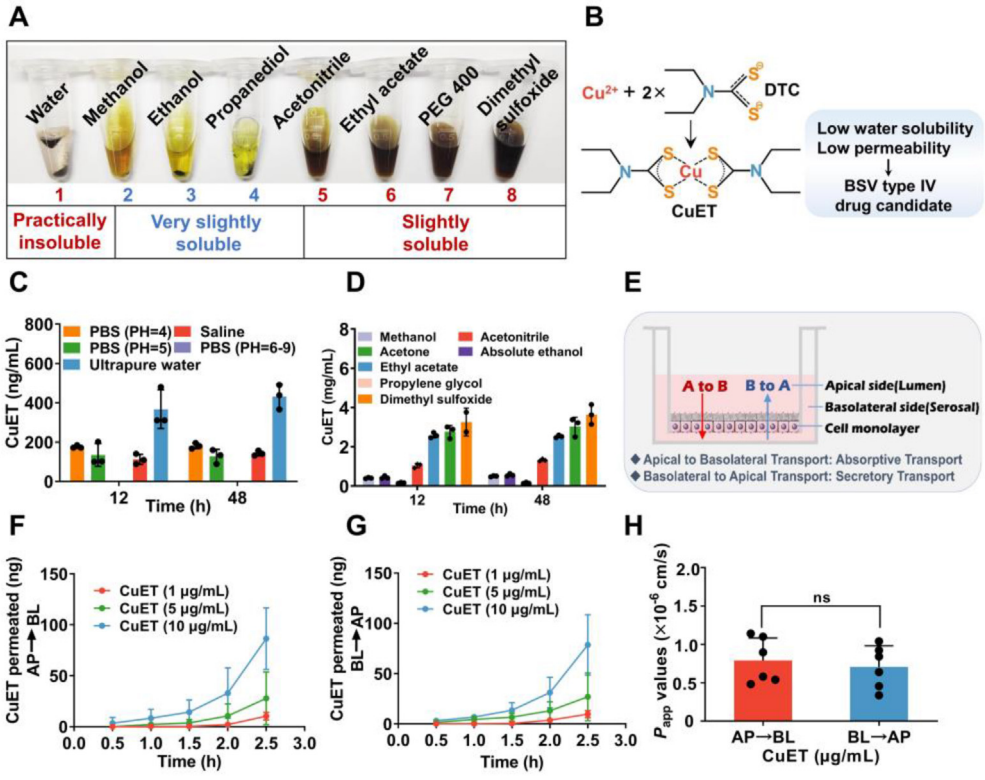

Figure 2 (A) Approximate solubility of CuET in water, organic solutions, and PEG400. (B) Schematic representation of CuET formation and BCS classification. (C, D) Equilibrium solubility of CuET in various common solvents. (E) Schematic representation of bidirectional transport in the Caco-2 cell monolayer model. (F) and (G) Bidirectional transmembrane transport of CuET. (H) P_{app} values of CuET transported across transwells for absorptive transport (AP→BL) and secretory transport (BL→AP). For panels Fig. 2C–G, $n = 3$ independent samples, for panel (H), $n = 6$ independent samples. Data are presented as mean ± SD, ns, $P > 0.05$.

To ensure that CuET did not significantly influence the cell model, we performed the MTT assay and measured the trans-epithelial electrical resistance (TEER, Supporting Information Figs. S5 and S6). These experiments confirmed that CuET had minimal effects on cell viability and the integrity of the cell monolayer at the tested concentrations. Collectively, these results demonstrate the low solubility and poor permeability of CuET, classifying it as a type IV drug candidate according to the bio-pharmaceutical classification system (BCS, Fig. 2B).

3.3. *Scaled-up preparation of CuET nanocrystals via metal coordination-mediated self-assembly*

The poor solubility of CuET in both aqueous solutions and organic solvents presents a significant challenge to its biomedical applications. Furthermore, as a BCS type IV drug candidate, CuET is predicted to have low bioavailability through conventional administration routes such as oral administration. In this regard, nano-drug delivery emerges as an excellent solution to enhance drug solubility and bioavailability. Among various nano-formulations, drug nanocrystals have garnered considerable attention due to their easy preparation and high drug loading capabilities compared to other nanoparticles[32]. Importantly, we have previously developed a metal coordination-driven self-assembly strategy for preparing nanocrystals of metallic drugs[34]. Taking inspiration from this approach, we generated CuET *in situ via* DTC and Cu^{2+} coordination, and subsequently prepared CuET nanocrystals (CuET NCs) with the assistance of polyvinyl pyrrolidone (PVP) as a stabilizer (Fig. 3A). This preparation process was completed within 1 min. Notably, since both DTC and Cu^{2+} are highly soluble in water, the use of organic solvents was unnecessary. Overall, this method is facile, environmentally friendly, and cost-effective, allowing for the

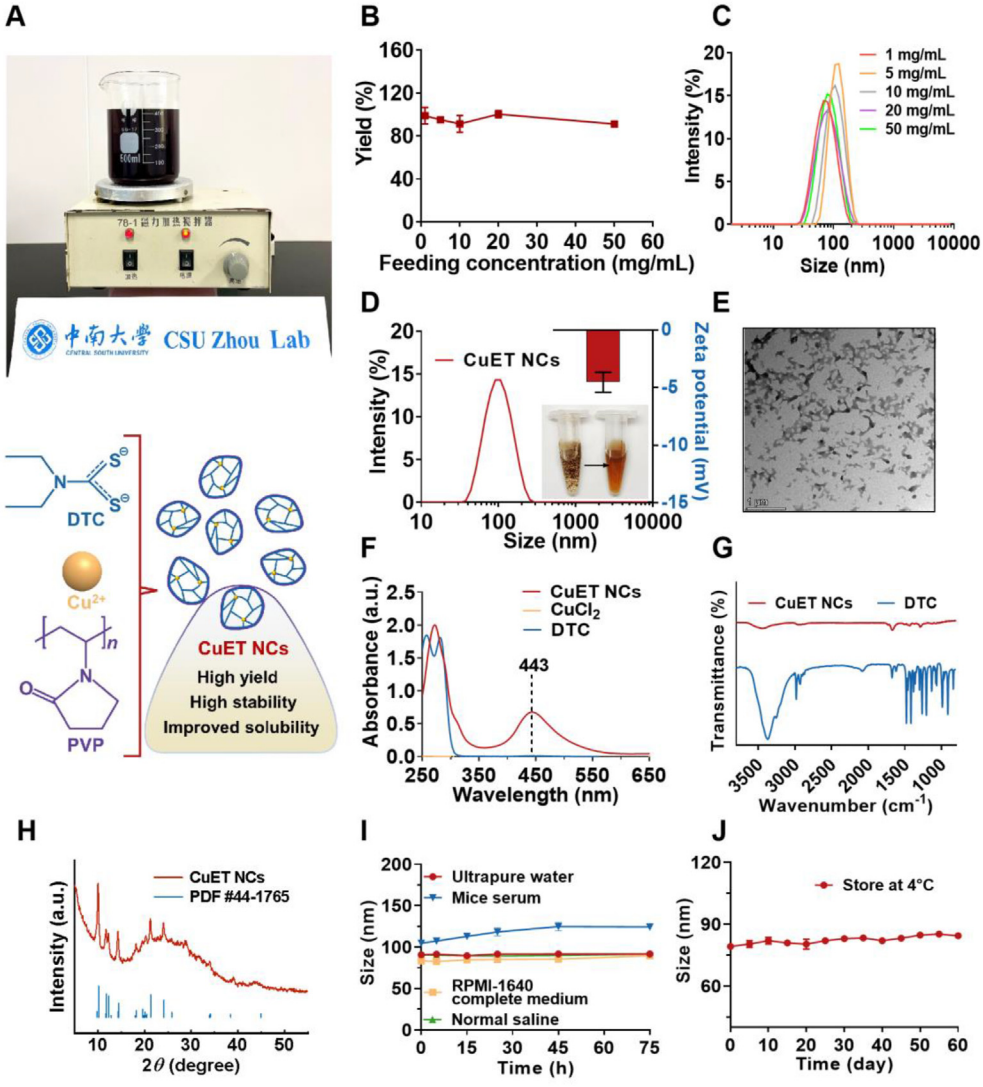

Figure 3 (A) Mass production of CuET NCs and preparation diagram. (B) Actual yield of CuET NCs with different mass concentrations at theoretical feeding concentration. (C) Size distribution diagram of CuET NCs at different mass concentrations. (D) The size distribution and ζ potential of CuET NCs. (E) TEM image of CuET NCs. (F) UV−Vis spectra of CuET NCs, $CuCl_2$, and DTC. (G) The FTIR spectra of CuET NCs and DTC. (H) The XRD pattern of CuET NCs. (I) The stability of CuET NCs in ultrapure water, saline, mice serum and RPMI 1640 complete medium for 75 h. (J) The long-term storage stability of CuET NCs at 4 °C. For panels Fig. 3B, I and J, $n = 3$ independent samples, data are presented as mean ± SD.

simple scale-up preparation of 500 mL of CuET NCs. Moreover, the concentration of the resulting CuET NCs can be easily adjusted by varying the feeding concentrations of DTC/Cu^{2+} (with a fixed 2/1, *mol/mol*), leading to homogeneous particle sizes (ranging from 65 to 150 nm) and a CuET yield exceeding 90% (Fig. 3B and C). No significant change of particle size was observed for different concentrations. Collectively, these results demonstrate that this CuET NCs preparation method is highly suitable for industrial production.

We then systematically characterized the CuET NCs. In absence of PVP, the formation of CuET rapidly aggregated to form insoluble precipitation (Fig. 3D). In presence of PVP, by contrast, a homogenous nanoparticle solution was obtained. The nanoparticles showed an average particle size were around 90 nm, with the surface charge of −4.5 mV (Fig. 3D). From TEM imaging (Fig. 3E), CuET NCs showed an irregular amorphous morphology, indicating a structure of metal coordination polymer. To confirm the *in situ* CuET generation, both UV−Vis and FTIR spectra were performed. CuET NCs showed a new characteristic UV−Vis absorbance peak at around 443 nm as compared to Cu^{2+} and DTC (Fig. 3F). On the other hand, the FTIR peaks at around 1140 cm^{-1} ($\nu_{C=S}$) and around 910 cm^{-1} ($\nu_{C\text{-}S}$) were seen in DTC but not in CuET NCs (Fig. 3G). These results suggested the coordination of C−S and C=S groups with Cu^{2+} to form CuET molecule. Moreover, the XRD pattern of CuET NCs displayed several obvious diffraction peaks at 10.1°, 11.9°, 12.4°, 14.4°, 21.4° and 24.1° (Fig. 3H), which was highly consistent with the first six strong peaks of CuET compound in standard library (numbered as #44-1765), confirming the crystalized structure of the nanoparticles. Besides, the complete XRD pattern results revealed the low crystallinity of CuET NCs (Supporting Information Fig. S7), which may explain the failure to observe the lattice in high-resolution TEM (HRTEM, Supporting Information Fig. S8). The colloidal stability of the CuET NCs was then explored, and no significant change of particle size was observed over 75 h under various media (Fig. 3I), indicating the potential of the nanoparticles for biological applications. In addition, the long-term stability was also studied, and such nanoparticles could be stored in water for at least 60 days at 4 °C without an obvious particle change (Fig. 3J).

3.4. Activity of CuET NCs in specifically inhibiting NLRP3 inflammasome activation

The above results have revealed that the enhancement of DSF-mediated pyroptosis inhibition by Cu^{2+} can be attributed to the *in situ* generation of CuET. Furthermore, the preparation of CuET nanocrystals (CuET NCs) allowed us to explore its broader anti-pyroptosis effects directly. We conducted experiments on primary mice macrophages, stimulating NLRP3 inflammasome activation through LPS+nigericin, LPS+ATP, and LPS+MSU, as well as non-canonical inflammasome activation through LPS transfection, NLRC4 inflammasome activation through flagellin transfection, and AIM2 inflammasome activation through poly(da:dT) transfection. Interestingly, we observed that CuET NCs specifically inhibited LDH and IL-1β secretion induced by NLRP3 inflammasome activation, while showing no significant effect on non-canonical inflammasome, NLRC4 inflammasome, or AIM2 inflammasome-induced responses. Similarly, CuET NCs had no effect on TNF-α and IL-6 secretion induced by all the inflammasome activation (Fig. 4A−D). In the case of NLRP3 inflammasome activation, CuET NCs completely inhibited GSDMD cleavage, whereas only a slight suppression was observed in the other three groups (Fig. 4E and F). These findings suggest that CuET NCs possess a specific inhibitory effect on NLRP3 inflammasome-induced pyroptosis, which exhibits some differences compared to DSF. In previous work, it showed that DSF could inhibit all inflammasome-induced pyroptosis through binding to GSDMD to block its pore formation. In our case, by contrast, CuET specifically inhibits NLRP3 inflammasome-induced pyroptosis probably through regulation of an upstream activation events of NLRP3 inflammasome (mentioned later). We also noticed that DSF achieved a robust inhibitory effect on pyroptosis at about 30 μmol/L, while CuET inhibits NLRP3 inflammasome at a lower dose of 2 μmol/L, this 15-fold changes are in accordance with the previous results that Cu^{2+} enhances the DSF's anti-pyroptosis effect, indicating that CuET exceeds DSF in the inhibition of NLRP3 inflammasome-induced pyroptosis. Therefore, CuET may implicated in NLRP3 inflammasome-associated diseases.

To further validate these observations, we assessed the effects of CuET NCs in human THP1 cells and obtained similar results, demonstrating the specific suppression of NLRP3 inflammasome-induced pyroptosis by CuET NCs (Fig. 4G and H). These results provide valuable insights into the activity of CuET NCs and their potential as a targeted therapy for NLRP3 inflammasome-associated diseases. The specific inhibition of NLRP3 inflammasome-induced pyroptosis by CuET NCs highlights their potential in modulating inflammatory responses, and suggests their utility in treating NLRP3 inflammasome-driven diseases, such as inflammatory disorders[42]. and autoimmune conditions[43].

3.5. CuET NCs inhibits NLRP3 inflammasome assembly by disrupting the association between NLRP3 and NEK7

To elucidate the underlying mechanism by which CuET NCs specifically inhibit NLRP3 inflammasome-induced pyroptosis, we conducted further investigations. We first examined the formation of ASC specks, which is a critical step in NLRP3 inflammasome assembly[42,44]. Immunofluorescence analysis revealed that CuET NCs treatment significantly reduced the percentage of cells containing ASC specks in response to ATP or nigericin stimulation (Fig. 5A and B). This observation was further supported by the detection of ASC oligomerization using disuccinimidyl suberate crosslinking (Fig. 5C and D). Thus, CuET NCs inhibit the formation of ASC specks, a key characteristic of NLRP3 inflammasome activation.

Previous studies have highlighted the importance of the interaction between NLRP3 and ASC in facilitating ASC speck formation[44]. To investigate whether CuET NCs affect this interaction, we performed immunoprecipitation and immunoblotting assays. The results demonstrated that CuET NCs significantly inhibited the interaction between NLRP3 and ASC (Fig. 5E and F). Furthermore, we explored the impact of CuET NCs on the interaction between NLRP3 and NEK7, a newly identified essential component of the NLRP3 inflammasome that promotes its assembly by connecting NLRP3 molecules together[45,46]. Remarkably, CuET NCs were found to disrupt the association between NLRP3 and NEK7 (Fig. 5G and H). These findings suggest that CuET NCs exert their specific inhibitory effect on NLRP3 inflammasome assembly by interfering with the interaction between NLRP3 and NEK7. These results provide insights into the mechanism of action of CuET NCs in specifically inhibiting NLRP3 inflammasome assembly. By disrupting the interaction between NLRP3 and NEK7, CuET NCs impair the

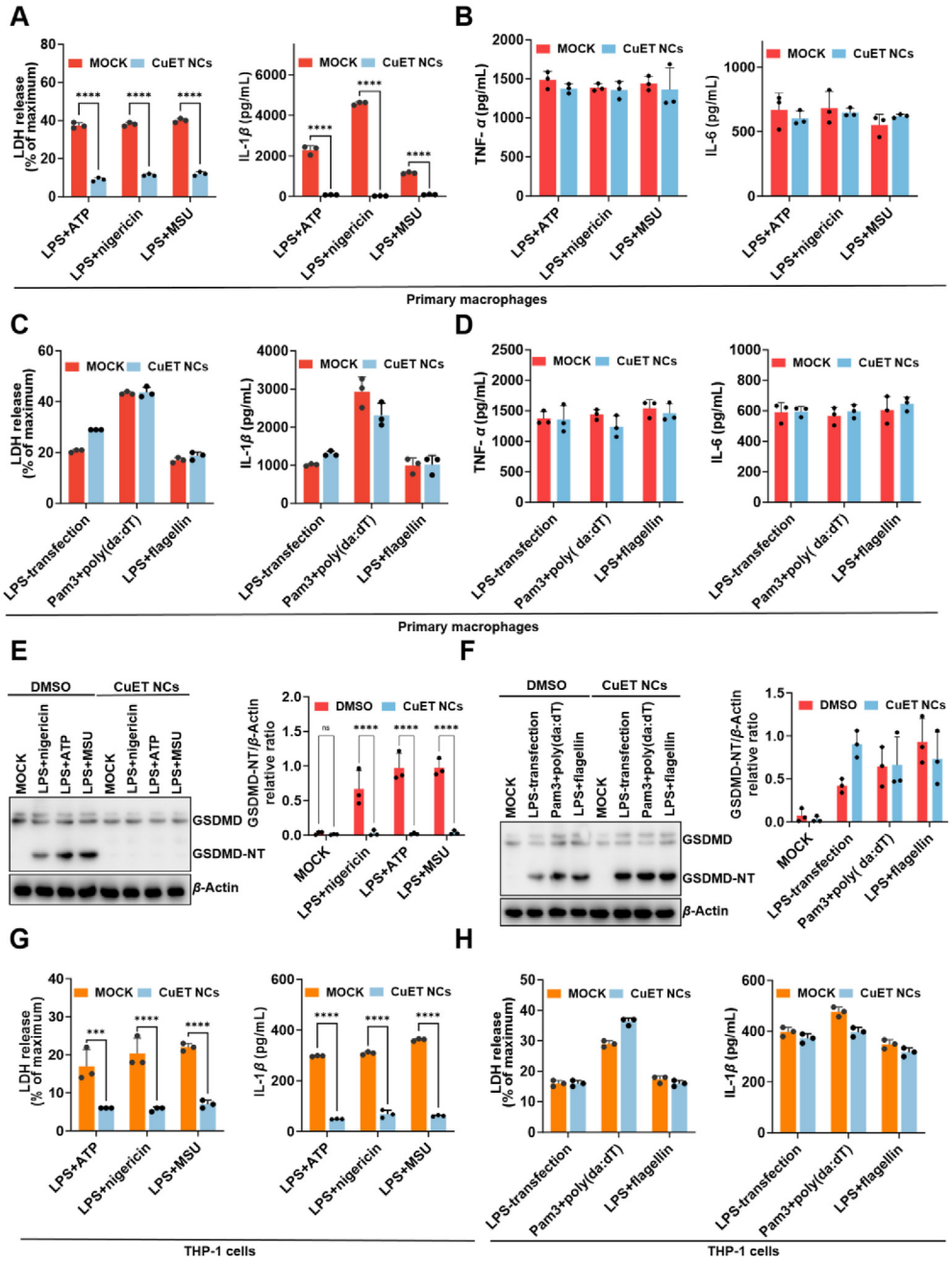

Figure 4 (A) and (B) LDH release and ELISA of IL-1β, TNF-α, IL-6 in supernatant from LPS-primed primary macrophages treated with a low dose of 2 μmol/L CuET NCs and stimulated with nigericin, ATP, MSU. (C, D) LDH release and Elisa of IL-1β, TNF-α, IL-6 in supernatant from LPS-primed primary macrophages treated with a low dose of 2 μmol/L CuET NCs and stimulated with nigericin, ATP, MSU, poly(da:dT), flagellin and transfected with LPS. (E, F) Primary macrophages were triggered as indicated. Cell lysates were subjected to Western blot analysis (left) and quantitative results (right). (G, H) LDH release and Elisa of IL-1β in supernatant from LPS-primed or pam3 -primed THP-1 treated with a low dose of 2 μmol/L CuET NCs and stimulated with nigericin, ATP, MSU, poly(da: dT), flagellin and transfected with LPS. Data are presented as mean ± SD ($n = 3$); *$P < 0.05$, **$P < 0.01$, and ****$P < 0.00001$, *vs.* indicated.

formation of ASC specks and consequently inhibit NLRP3 inflammasome-mediated pyroptosis.

3.6. *In vivo validation the anti-pyroptosis activity of CuET NCs*

To assess the *in vivo* performance of CuET NCs, we investigated their therapeutic potential in a LPS-induced sepsis model in mice. This model is widely used for studying the pharmacodynamics of anti-pyroptosis drugs due to its high success rate, simplicity, and reproducibility[47].

The biosafety of CuET NCs was thoroughly investigated through a hemolysis test, with deionized water and saline serving as positive and negative controls, respectively. The hemolysis rate of CuET NCs was calculated to be 2.08%, confirming their safety for intraperitoneal injection (Supporting Information Fig. S9). We monitored the changes in body temperature using infrared

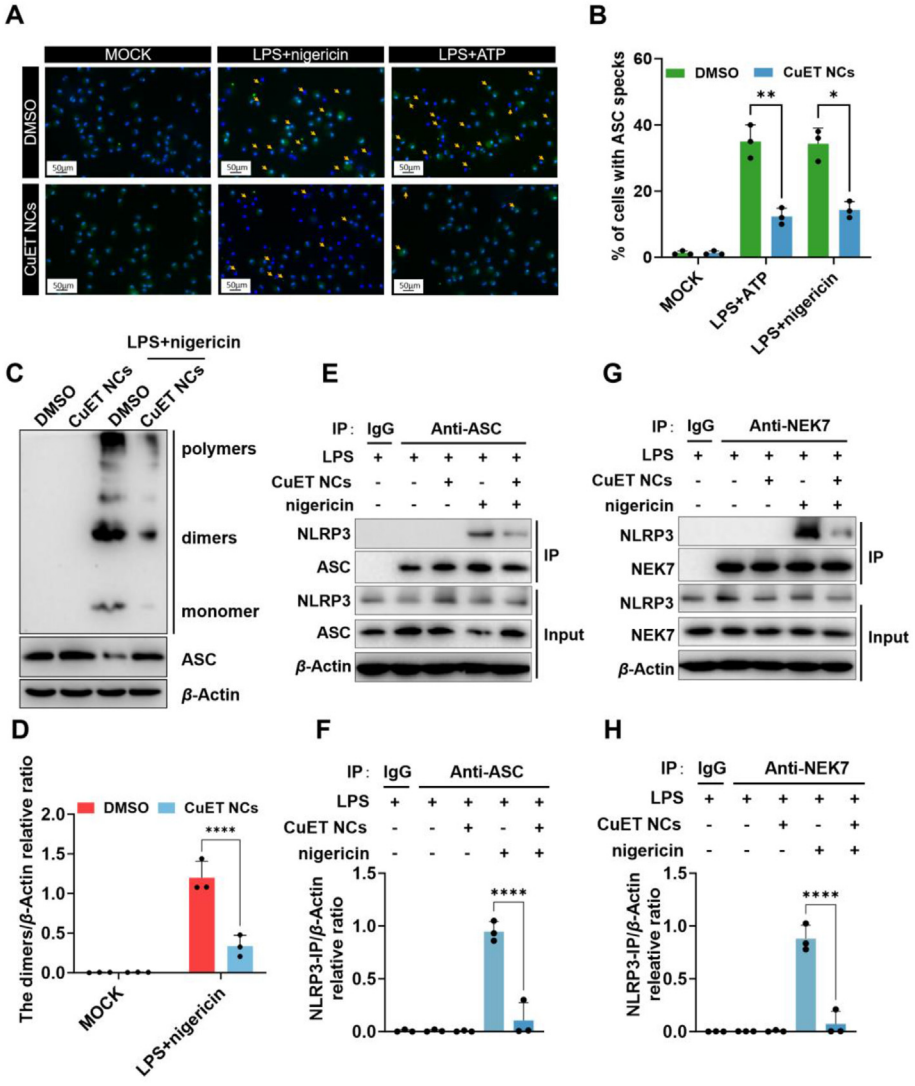

Figure 5 (A) and (B) Immunofluorescence microscopy analysis of primary macrophages treated with LPS- ATP or LPS-nigericin with or without CuET NCs treatment. (A) Representative images show the subcellular distribution of ASC specks. Scale bar = 50 μm. (B)Quantification of ASC speck formation based on the number of cells with ASC specks. (C, D) Immunoblot analysis and quantitative results of ASC oligomerization in cross-linked cytosolic pellets of LPS-primed primary macrophages treated with CuET NCs or DMSO and then stimulated with nigericin. (E) and (F) Immunoblot analysis and quantitative results of the interaction between NLRP3 and ASC in LPS-primed primary macrophages treated with CuET NCs and then stimulated with nigericin. (G, H) Immunoblot analysis and quantitative results of the interaction between NEK7 and NLRP3 in LPS-primed primary macrophages treated with CuET NCs and then stimulated with nigericin. Data are presented as mean ± SD ($n = 3$); *$P < 0.05$, **$P < 0.01$, and ****$P < 0.00001$, *vs.* indicated.

thermography, as hypothermia has been associated with increased mortality and organ failure in septic patients[48]. For 4 h after intraperitoneal injection of LPS (20 mg/kg), the body temperature of mice in the LPS group significantly decreased compared to the other three groups (Fig. 6A). By 13 h after modeling, the average body temperature of mice in the LPS group had decreased by 3.4 °C, while in the 1 and 2 mg/kg CuET NCs-treated groups, the decreases were 1.63 and 0.52 °C, respectively (Fig. 6A). These results demonstrate the protective effect of CuET NCs in alleviating hypothermia in septic mice.

We further investigated whether CuET NCs could ameliorate the inflammatory responses and organ damage associated with disease progression and immune impairment in the sepsis model. Following LPS injection at a dose of 25 mg/kg, the levels of inflammatory cytokines, including IL-1β and IL-6, were significantly elevated (Fig. 6B and C). Treatment with 1 or 2 mg/kg CuET NCs resulted in a 47% and 60% decrease, respectively, in the serum levels of IL-1β compared to the LPS group, while IL-6 levels remained unaffected (Fig. 6B and C). This differential effect of CuET NCs on the two cytokines may be explained by the fact that IL-6 is not specifically dependent on NLRP3 inflammasome activation, unlike IL-1β. Histological examination of lung and liver tissues using H&E staining revealed alveolar wall thickening, inflammatory cell infiltration in the lung, and hepatocyte edema, necrosis, and vacuolation in the liver in the LPS-treated group (Fig. 6D). However, in the CuET NCs-treated group, these pathological changes in the lung and liver were markedly alleviated (Fig. 6D). Together, these findings demonstrate the promising

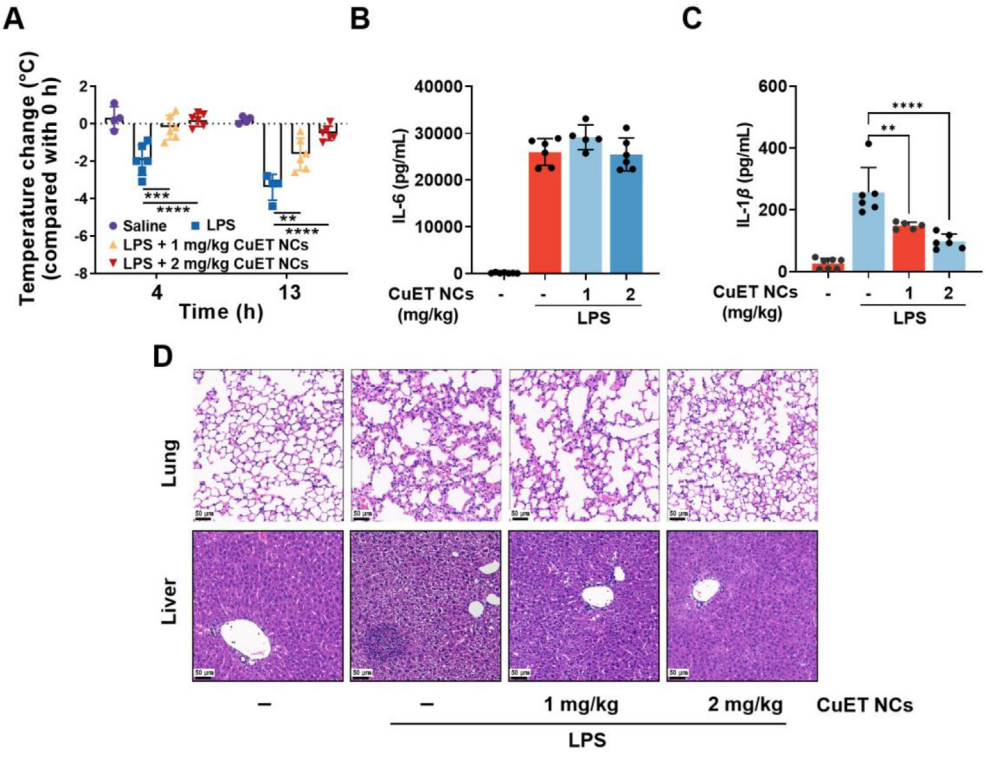

Figure 6 (A) Changes in body temperature of septic mice with different treatments. (B, C) Serum levels of IL-1β and IL-6 in mice. (D) Histological sections of lung and liver stained with H&E. Scale bar = 50 μm. For Fig. 6A–C, $n \geq 4$ per group, data are presented as mean ± SD, $^{**}P < 0.01$ and $^{****}P < 0.00001$, *vs.* indicated.

therapeutic potential of CuET NCs in the LPS-induced sepsis model by mitigating hypothermia, reducing the levels of NLRP3 inflammasome-specific inflammatory factor IL-1β, and ameliorating organ damage.

3.7. *Biopharmaceutical characteristics of CuET NCs via oral administration*

Having confirmed the bioactivity of CuET both *in vitro* and *in vivo*, and we next explored the real application of CuET NCs *via* the most convenient treatment format of oral administration. As the first step, the biopharmaceutical characteristics of CuET NCs were studied. For this purpose, the quantification CuET in blood and tissue was the most important task. However, we observed a gradual decrease in the signal of CuET over time in both plasma and BSA matrices, despite its stability in water (Fig. 7A and B, and Supporting Information Fig. S10). This decline suggested strong protein binding of the drug.

To explore the binding mechanism, we employed fluorescence and circular dichroism (CD) spectra analysis on BSA. The fluorescence signal of BSA originates from Trp, Tyr, and Phe residues, with Trp contributing the most. When excited at 280 nm, BSA exhibited a strong fluorescence emission peak at 340 nm. Incubation of BSA with CuET resulted in a progressive decrease in its fluorescence intensity at higher CuET concentrations (Fig. 7C and Supporting Information Fig. S11). The three-dimensional fluorescence spectra of BSA also showed a similar decrease (Supporting Information Fig. S12). Importantly, there was no significant shift in the emission wavelength, indicating that CuET interacts with BSA and quenches its intrinsic fluorescence. To gain mechanistic insights, we measured the fluorescence decrease at both 298 and 310 K and analyzed the fluorescence quenching data using the Stern–Volmer equation. Both curves yielded linear plots (Fig. 7D, Supporting Information Table S5), from which the fluorescence quenching constants K_q (L/mol/s) were calculated as $(1.35 \pm 0.35) \times 10^{13}$ and $(1.17 \pm 0.16) \times 10^{13}$ at 298 and 310 K, respectively (Fig. 7E). These constants exceeded the maximum diffusion constant of biomacromolecules (2×10^{10})[49]. Indicating that the interaction between CuET and BSA primarily involved static quenching through the formation of non-luminescent complexes.

We further analyzed the binding between CuET and BSA using a double logarithmic regression equation. The plots of log $[(F_0-F)/F]$ *versus* log$[Q]$ also showed linear relationships (Fig. 7F, Supporting Information Table S6), and the binding constants Ka (L/mol) at 298 and 310 K were determined as $(1.37 \pm 0.39) \times 10^4$ and $(5.38 \pm 2.76) \times 10^4$, respectively (Fig. 7G). The binding site number ranged from 0.81 to 1.02, suggesting that each BSA molecule binds to one CuET molecule with moderate affinity. The strength and reversibility of drug–protein binding are important factors that influence the biopharmaceutical properties of drugs *in vivo*. Weak binding may result in inadequate transport, while strong binding can lead to very low concentrations of unbound drug molecules. Therefore, the moderate binding capacity of CuET is a suitable characteristic for *in vivo* medication. Additionally, we analyzed the secondary structure of BSA using CD spectroscopy. The presence of CuET caused a reduction in the peak height amplitude of BSA (Fig. 7H), indicating a decrease in the ellipticity of BSA and partial unfolding of its α-helical structure upon binding to CuET.

Based on the above results, it appears that CuET exhibits relatively stronger binding affinity towards BSA at higher

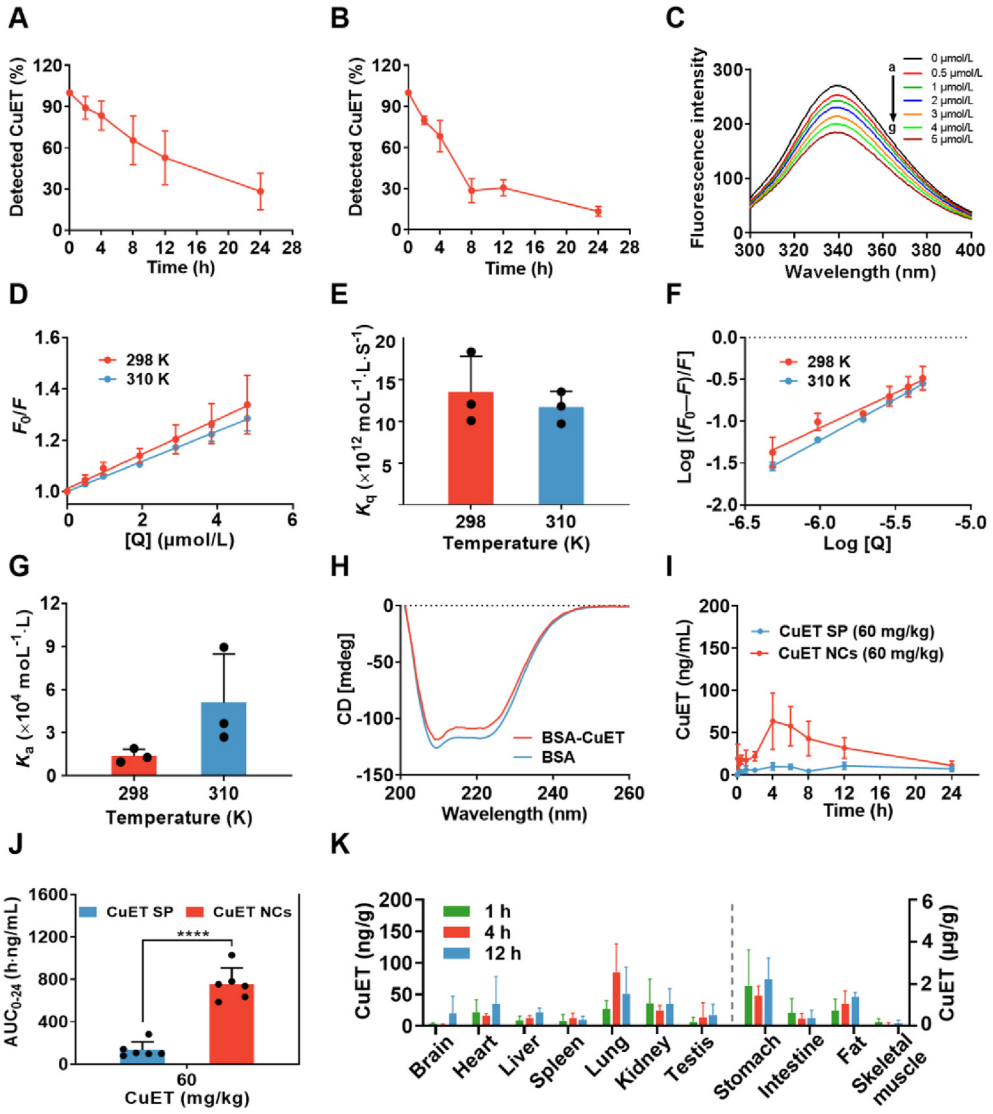

Figure 7 (A, B) Stability of CuET in plasma (A) or BSA matrixes (B, 50 mg/kg) at room temperature. (C) Fluorescence quenching spectra of BSA in the presence of CuET at different concentrations (a−g, concentrations of CuET were 0, 0.5, 1, 2, 3, 4, and 5 μmol/L respectively, T = 298 K). (D) and (F) Stern−Volmer and log (F_0−F)/F *versus* logQ plots describing BSA quenching by CuET at 298 K, 310 K, [Q] is concentration of the quencher. (E) Fluorescence Quenching Rate Constants (K_q) of BSA on complexation with CuET at 298 K, 310 K. (G) Binding constant (K_a) of BSA on complexation with CuET at 298 K, 310 K. (H) CD spectra of BSA in the presence of CuET at ratio of 1/1 (n/n, protein/complex) measured in the far-UV region (200−260 nm). (I) Mean plasma concentration−time profiles of CuET SP and CuET NCs following oral administration at a dose of 60 mg/kg in Sprague−Dawley rats. (J) Area under the concentration−time curves ($AUC_{0\text{-}24}$) of CuET and CuET NCs. (K) Biodistribution of CuET NCs (60 mg/kg) in major organs at various times after administration. The dotted line in the figure divides the left and right y-axes. For Fig. 4A, B and D−G, n = 3 independent samples. For Fig. 4I−K, n = 6 independent samples. Data presented as mean ± standard deviation (SD), ****P < 0.00001, *vs.* indicated.

temperatures. To avoid interference from biological matrices, the CuET detection method was established under a salt ice bath. Following oral administration of CuET NCs (60 mg/kg), the concentration of the drug in the blood gradually increased, reaching a T_{max} of 4.67 ± 0.94 h, followed by a plateau phase with a $T_{1/2}$ of 8.51 ± 1.68 h (Fig. 7I). In comparison, the blood drug concentration was much lower for CuET SP. Consequently, CuET NCs exhibited a 6-fold higher relative area under the concentration−time curve ($AUC_{0\text{-}24}$) than its free drug counterpart (Fig. 7J), indicating an improved bioavailability of the nanocrystal formulation. With this significant enhancement in bioavailability achieved by CuET NCs, we further investigated the tissue drug concentration at 1 h (absorption phase), 4 h (distribution phase), and 12 h (elimination phase) to understand the distribution pattern and accumulation of CuET NCs in the body. Interestingly, CuET primarily distributed in the stomach, intestine, adipose tissue, and skeletal muscle after oral administration, and the drug remained in these tissues for at least 12 h (Fig. 7K). It is worth noting that CuET exhibited low concentrations in major metabolic organs such as the liver and kidney, which may be attributed to rapid metabolism and elimination when CuET is transported to these organs.

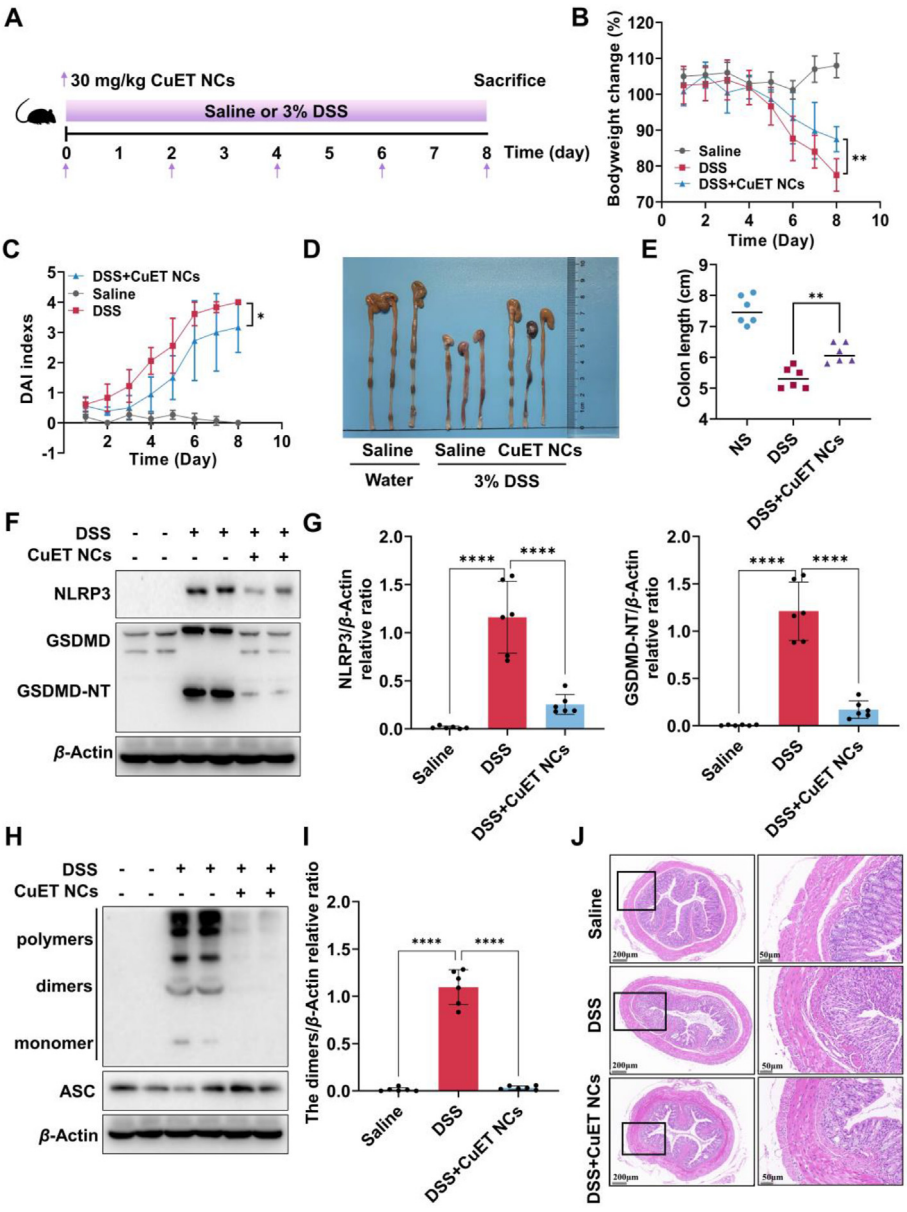

Figure 8 (A) Experimental design depicting the DSS-induced colitis mouse model and CuET NCs treatment. (B) Changes in body weight expressed as a percentage of bodyweight change ($n \geq 5$ per group). (C) Disease Activity Index (DAI) calculated based on weight loss, diarrhea, and gross bleeding ($n \geq 5$ per group). (D, E) Gross morphology of colons from C57BL/6 mice. Colon length was measured on day 8 ($n \geq 5$). (F, G) Immunoblot analysis and quantitative results of NLRP3, and GSDMD. Data were normalized to β-actin expression. (H, I) Immunoblot analysis and quantitative results of ASC oligomerization in cross-linked cytosolic pellets of DSS-induced colitis treated with or without CuET NCs treatment. (J) H&E-stained images of colon sections from DSS-induced colitis mice treated with or without CuET NCs. The results of (B) and (C) are expressed as mean ± SD ($n = 3$), $^{**}P < 0.01$ and $^{****}P < 0.00001$, *vs.* indicated.

3.8. Therapeutic efficacy of CuET NCs in DSS-induced colitis murine model

The biodistribution characteristics mentioned above also indicate the potential clinical applications of CuET. Previously, we have explored CuET for the treatment of breast cancer due to its anti-tumor activity and its ability to accumulate in fatty tissues[34]. In this study, we have demonstrated the anti-pyroptosis activity of CuET by specifically targeting the NLRP3 inflammasome. Given its high distribution in the intestine, CuET NCs could be a promising candidate for the treatment of inflammatory bowel diseases (IBDs). IBDs encompass chronic inflammatory disorders primarily including ulcerative colitis (UC) and Crohn's disease (CD). The development of IBDs is influenced by genetics, immune responses, and environmental triggers[50]. Numerous studies have revealed the involvement of the NLRP3 inflammasome in the pathogenesis of IBDs[51−53]. Human studies have found that the NLRP3 inflammasome is activated in UC and CD[51]. In murine models, deficiencies in NLRP3, ASC, or caspase-1, which are components of the NLRP3 inflammasome, have shown attenuation of inflammatory colitis[52]. Additionally, targeting the NLRP3 inflammasome with small molecules has demonstrated the ability to alleviate colitis symptoms[54−57] Therefore, based on these

findings, we have decided to further investigate the potential of CuET in the treatment of IBDs.

To evaluate the therapeutic efficacy of CuET NCs in a DSS-induced colitis murine model, mice were administered 3% DSS in their drinking water for 9 days to induce acute colitis (Fig. 8A). CuET NCs were orally injected every other day from Day 0 to Day 8, and clinically relevant parameters such as body weight, presence of grossly bloody stools, and stool consistency were recorded daily. Compared to the control group of normal mice, the DSS-induced model mice experienced a 20% weight loss. However, treatment with CuET NCs significantly ameliorated the weight loss (Fig. 8B). Disease activity index (DAI), a summary score considering weight loss, diarrhea, and gross bleeding, was used to assess the severity of colitis (Fig. 8C). Consistently, DSS-fed mice exhibited severe weight loss, diarrhea, and high DAI scores, which were reduced after treatment with CuET NCs. The colon length, an indicator of colitis severity, was significantly decreased in the model mice but improved with CuET NCs treatment (Fig. 8D and E). Encouraged by these positive outcomes, we further investigated the underlying mechanisms by examining the influence of CuET NCs on NLRP3 inflammasome activity in the DSS-induced model. Intestinal expression of NLRP3 was enhanced in mice fed with 3% DSS, accompanied by an increase in GSDMD-NT, a key executor of pyroptosis. However, CuET NCs treatment led to a reduction in NLRP3 and GSDMD-NT expression (Fig. 8F and G). Moreover, CuET NCs inhibited ASC speck formation in colon tissues of DSS-induced colitis (Fig. 8H and I). These findings collectively suggested that CuET NCs suppress NLRP3 inflammasome activation in the DSS-induced colitis model.

To further confirm the efficacy, histological examination using hematoxylin and eosin (H&E) staining was performed. Severe mucosal damage, gland destruction, and infiltration of mononuclear cells were observed in the colon specimens of DSS-fed mice. In contrast, mice treated with CuET NCs exhibited intact colonic architecture without mucosal damage and reduced mononuclear cell infiltration (Fig. 8J). The concentration of CuET in the mouse body was found to be very low 48 hs after the administration of CuET NCs (Supporting Information Tables S7 and S8). Additionally, there were no significant pathological changes observed in the major organs (heart, liver, spleen, lungs, and kidneys), as shown in Supporting Information Fig. S13. These results suggest that CuET NCs are highly biocompatible and were completely cleared from the body.

The facile scalable preparation, convenient administration, biocompatibility, and robust efficacy of this nanomedicine highlight its promising potential for clinical translation in managing both cancer and NLRP3 inflammasome-related inflammatory diseases.

4. Conclusions

In conclusion, our study provides valuable insights into the sensitizing effect of Cu^{2+} on the anti-pyroptotic activity of DSF through the generation of CuET. We demonstrate that CuET exhibits significantly enhanced anti-pyroptotic activity compared to DSF by specifically targeting and inhibiting the assembly of NLRP3 inflammasomes through disruption of the NLRP3-NEK7 association. This contrasts with DSF, which inhibits all inflammasome-induced pyroptosis by binding to GSDMD and blocking pore formation. Therefore, CuET holds promise for the treatment of NLRP3 inflammasome-associated diseases. Despite the initial limitations of CuET, including poor solubility and permeability, we successfully addressed these druggability challenges by developing CuET nanocrystals (CuET NCs) using a scalable and productive method. The CuET NCs exhibited a remarkable 6-fold improvement in bioavailability compared to CuET SP. Furthermore, we observed high biodistribution of CuET NCs in the intestine, highlighting their potential application in the treatment of inflammatory bowel diseases (IBDs). To evaluate their *in vivo* efficacy, we utilized a DSS-induced colitis murine model and demonstrated the potent anti-inflammatory effects and amelioration of colitis symptoms by CuET NCs. This work explicitly elucidates the mechanism of action of CuET in inhibiting NLRP3 inflammasome-induced pyroptosis, which presents a novel therapeutic strategy for NLRP3 inflammasome-associated diseases. Additionally, the development of CuET NCs addresses the druggability limitations of CuET, enhancing its bioavailability and demonstrating its potential for clinical translation. These findings lay the foundation for further development and clinical application of CuET NCs in the treatment of inflammatory bowel diseases and other pyroptosis-related disorders.

Acknowledgments

This work was supported by National Key Research and Development Program of China (2021YFC2500802), National Natural Science Foundation of China (Nos. 82071986, 82073799, 81771827, 82272207, and 82202398), Natural Science Foundation of Hunan Province China (Nos. 2021JJ20084 and 2021JJ20090), the Science and Technology Innovation Program of Hunan Province (2021RC3020, China), the Central South University Graduate Students Independent Exploration and Innovation Project (No. 2021zzts0984, China), and the Wisdom Accumulation and Talent Cultivation Project of the Third Xiangya Hospital of Central South University (China).

Author contributions

Wenhu Zhou and Kai Zhao designed the research. Xueming Xu, Yuanfeng Han and Jiali Deng carried out the experiments and performed data analysis. Shengfeng Wang and Shijie Zhuo participated part of the experiments. Xueming Xu, Yuanfeng Han and Jiali Deng wrote the manuscript. Wenhu Zhou and Kai Zhao revised the manuscript. All the authors have read and approved the final manuscript.

Conflicts of interest

The authors declare no conflicts of interest.

Appendix A. Supporting information

Supporting data to this article can be found online at https://doi.org/10.1016/j.apsb.2024.03.003.

References

1. Chong CR, Sullivan DJ. New uses for old drugs. *Nature* 2007;**448**:645–6.
2. Zhao P, Tang X, Huang Y. Teaching new tricks to old dogs: a review of drug repositioning of disulfiram for cancer nanomedicine. *VIEW* 2021;**2**:20200127.

3. Fuller RK, Branchey L, Brightwell DR, Derman RM, Emrick CD, Iber FL, et al. Disulfiram treatment of alcoholism. A veterans administration cooperative study. *JAMA* 1986;**256**:1449−55.
4. Caminear MW, Harrington BS, Kamdar RD, Kruhlak MJ, Annunziata CM. Disulfiram transcends ALDH inhibitory activity when targeting ovarian cancer tumor-initiating cells. *Front Oncol* 2022;**12**:762820.
5. Mohammad IS, Teng C, Chaurasiya B, Yin L, Wu C, He W. Drug-delivering-drug approach-based codelivery of paclitaxel and disulfiram for treating multidrug-resistant cancer. *Int J Pharm* 2019; **557**:304−13.
6. Kannappan V, Ali M, Small B, Rajendran G, Elzhenni S, Taj H, et al. Recent advances in repurposing disulfiram and disulfiram derivatives as copper-dependent anticancer agents. *Front Mol Biosci* 2021;**8**:741316.
7. Lu Y, Pan Q, Gao W, Pu Y, Luo K, He B, et al. Leveraging disulfiram to treat cancer: mechanisms of action, delivery strategies, and treatment regimens. *Biomaterials* 2022;**281**:121335.
8. Oliveri V. Selective Targeting of cancer cells by copper ionophores: an overview. *Front Mol Biosci* 2022;**9**:841814.
9. Li H, Wang J, Wu C, Wang L, Chen ZS, Cui W. The combination of disulfiram and copper for cancer treatment. *Drug Discov Today* 2020; **25**:1099−108.
10. Wang NN, Wang LH, Li Y, Fu SY, Xue X, Jia LN, et al. Targeting ALDH2 with disulfiram/copper reverses the resistance of cancer cells to microtubule inhibitors. *Exp Cell Res* 2018;**362**:72−82.
11. Li H, Wang J, Wu C, Wang L, Chen ZS, Cui W. The combination of disulfiram and copper for cancer treatment. *Drug Discov Today* 2020; **25**:1099−108.
12. Xu B, Shi P, Fombon IS, Zhang Y, Huang F, Wang W, et al. Disulfiram/copper complex activated JNK/c-jun pathway and sensitized cytotoxicity of doxorubicin in doxorubicin resistant leukemia HL60 cells. *Blood Cells Mol Dis* 2011;**47**:264−9.
13. Li Y, Chen F, Chen J, Chan S, He Y, Liu W, et al. Disulfiram/copper induces antitumor activity against both nasopharyngeal cancer cells and cancer-associated fibroblasts through ROS/MAPK and ferroptosis pathways. *Cancers (Basel)* 2020;**12**:138.
14. Loo TW, Bartlett MC, Clarke DM. Disulfiram metabolites permanently inactivate the human multidrug resistance P-glycoprotein. *Mol Pharm* 2004;**1**:426−33.
15. Li Y, Fu SY, Wang LH, Wang FY, Wang NN, Cao Q, et al. Copper improves the anti-angiogenic activity of disulfiram through the EGFR/Src/VEGF pathway in gliomas. *Cancer Lett* 2015;**369** :86−96.
16. Li Y, Wang LH, Zhang HT, Wang YT, Liu S, Zhou WL, et al. Disulfiram combined with copper inhibits metastasis and epithelial-mesenchymal transition in hepatocellular carcinoma through the NF-κB and TGF-β pathways. *J Cell Mol Med* 2018;**22**:439−51.
17. Skrott Z, Mistrik M, Andersen KK, Friis S, Majera D, Gursky J, et al. Alcohol-abuse drug disulfiram targets cancer *via* p97 segregase adaptor NPL4. *Nature* 2017;**552**:194−9.
18. Pan M, Zheng Q, Yu Y, Ai H, Xie Y, Zeng X, et al. Seesaw conformations of Npl4 in the human p97 complex and the inhibitory mechanism of a disulfiram derivative. *Nat Commun* 2021;**12**:121.
19. Hu JJ, Liu X, Xia S, Zhang Z, Zhang Y, Zhao J, et al. FDA-approved disulfiram inhibits pyroptosis by blocking gasdermin D pore formation. *Nat Immunol* 2020;**21**:736−45.
20. Ou AT, Zhang JX, Fang YF, Wang R, Tang XP, Zhao PF, et al. Disulfiram-loaded lactoferrin nanoparticles for treating inflammatory diseases. *Acta Pharmacol Sin* 2021;**42**:1913−20.
21. Chen Y, Shui M, Yuan Q, Vong CT, Yang Z, Chen Z, et al. Wielding the double-edged sword: redox drug delivery systems for inflammatory bowel disease. *J Control Release* 2023;**358**:510−40.
22. Cookson BT, Brennan MA. Pro-inflammatory programmed cell death. *Trends Microbiol* 2001;**9**:113−4.
23. Rathinam VAK, Zhao Y, Shao F. Innate immunity to intracellular LPS. *Nat Immunol* 2019;**20**:527−33.
24. Xia S, Hollingsworth LRt, Wu H. Mechanism and regulation of gasdermin-mediated cell death. *Cold Spring Harb Perspect Biol* 2020; **12**:a036400.
25. Jorgensen I, Rayamajhi M, Miao EA. Programmed cell death as a defence against infection. *Nat Rev Immunol* 2017;**17**:151−64.
26. Lieberman J, Wu H, Kagan JC. Gasdermin D activity in inflammation and host defense. *Sci immunol* 2019;**4**:eaav1447.
27. Wang R, Shen J, Yan H, Gao X, Dong T, Wang P, et al. The evolving role of disulfiram in radiobiology and the treatment of breast cancer. *OncoTargets Ther* 2020;**13**:10441−6.
28. Liu T, Wang P, Cong M, Zhao X, Zhang D, Xu H, et al. Diethyldithiocarbamate, an anti-abuse drug, alleviates steatohepatitis and fibrosis in rodents through modulating lipid metabolism and oxidative stress. *Br J Pharmacol* 2018;**175**:4480−95.
29. Nagai N, Murao T, Okamoto N, Ito Y. Disulfiram reduces elevated blood glucose levels in Otsuka Long-Evans Tokushima Fatty (OLETF) rats, a model of type 2 diabetes. *J Oleo Sci* 2009;**58**:485−90.
30. Li C, Li L, Lan T. Co-treatment with disulfiram and glycyrrhizic acid suppresses the inflammatory response of chondrocytes. *J Orthop Surg Res* 2021;**16**:132.
31. Bilsel Y, Bugra D, Yamaner S, Bulut T, Cevikbas U, Turkoglu U. Could honey have a place in colitis therapy? Effects of honey, prednisolone, and disulfiram on inflammation, nitric oxide, and free radical formation. *Dig Surg* 2002;**19**:306−11.
32. Mohammad IS, Hu H, Yin L, He W. Drug nanocrystals: fabrication methods and promising therapeutic applications. *Int J Pharm* 2019; **562**:187−202.
33. Pu Y, Fan X, Zhang Z, Guo Z, Pan Q, Gao W, et al. Harnessing polymer-derived drug delivery systems for combating inflammatory bowel disease. *J Control Release* 2023;**354**:1−18.
34. Peng Y, Liu P, Meng Y, Hu S, Ding J, Zhou W. Nanoscale copper(II)-diethyldithiocarbamate coordination polymer as a drug self-delivery system for highly robust and specific cancer therapy. *Mol Pharm* 2020;**17**:2864−73.
35. Han L, Zhao Y, Yin L, Li R, Liang Y, Huang H, et al. Insulin-loaded pH-sensitive hyaluronic acid nanoparticles enhance transcellular delivery. *AAPS PharmSciTech* 2012;**13**:836−45.
36. Shrestha N, Shahbazi MA, Araújo F, Zhang H, Mäkilä EM, Kauppila J, et al. Chitosan-modified porous silicon microparticles for enhanced permeability of insulin across intestinal cell monolayers. *Biomaterials* 2014;**35**:7172−9.
37. Gałczyńska K, Ciepluch K, Kurdziel K, Biehl R, Arabski M. Spectroscopic and small-angle X-ray scattering analysis of binding between copper(II)-1-allylimidazole complex, a potential anti-tumor agent, and bovine serum albumin. *Bioorg Chem* 2021;**116**:105327.
38. Zhang L, Liu Y, Wang Y. Interaction between an (−)-epigallocatechin-3-gallate-copper complex and bovine serum albumin: fluorescence, circular dichroism, HPLC, and docking studies. *Food Chem* 2019;**301**: 125294.
39. Cooper HS, Murthy SN, Shah RS, Sedergran DJ. Clinicopathologic study of dextran sulfate sodium experimental murine colitis. *Lab Invest* 1993;**69**:238−49.
40. Alex P, Zachos NC, Nguyen T, Gonzales L, Chen TE, Conklin LS, et al. Distinct cytokine patterns identified from multiplex profiles of murine DSS and TNBS-induced colitis. *Inflamm Bowel Dis* 2009;**15**:341−52.
41. Deigendesch N, Zychlinsky A, Meissner F. Copper regulates the canonical NLRP3 inflammasome. *J Immunol* 2018;**200**:1607−17.
42. Davis BK, Wen H, Ting JP. The inflammasome NLRs in immunity, inflammation, and associated diseases. *Annu Rev Immunol* 2011;**29**: 707−35.
43. Shen HH, Yang YX, Meng X, Luo XY, Li XM, Shuai ZW, et al. NLRP3: a promising therapeutic target for autoimmune diseases. *Autoimmun Rev* 2018;**17**:694−702.
44. Fernandes-Alnemri T, Wu J, Yu JW, Datta P, Miller B, Jankowski W, et al. The pyroptosome: a supramolecular assembly of ASC dimers mediating inflammatory cell death *via* caspase-1 activation. *Cell Death Differ* 2007;**14**:1590−604.

45. He Y, Zeng MY, Yang D, Motro B, Núñez G. NEK7 is an essential mediator of NLRP3 activation downstream of potassium efflux. *Nature* 2016;**530**:354−7.
46. Schmid-Burgk JL, Chauhan D, Schmidt T, Ebert TS, Reinhardt J, Endl E, et al. A genome-wide CRISPR (clustered regularly interspaced short palindromic repeats) screen identifies NEK7 as an essential component of NLRP3 inflammasome activation. *J Biol Chem* 2016;**291**:103−9.
47. Stortz JA, Raymond SL, Mira JC, Moldawer LL, Mohr AM, Efron PA. Murine models of sepsis and trauma: can we bridge the gap?. *ILAR J* 2017;**58**:90−105.
48. Kushimoto S, Gando S, Saitoh D, Mayumi T, Ogura H, Fujishima S, et al. The impact of body temperature abnormalities on the disease severity and outcome in patients with severe sepsis: an analysis from a multicenter, prospective survey of severe sepsis. *Crit Care (London, England)* 2013;**17**:R271.
49. Jayabharathi J, Thanikachalam V, Srinivasan N, Perumal MV. Luminescent study on the binding interaction of bioactive imidazole with bovine serum albumin-A static quenching mechanism. *Spectrochim Acta* 2011;**84**:233−7.
50. Kaplan GG. The global burden of IBD: from 2015 to 2025. *Nat Rev Gastroenterol Hepatol* 2015;**12**:720−7.
51. Zhen Y, Zhang H. NLRP3 inflammasome and inflammatory bowel disease. *Front Immunol* 2019;**10**:276.
52. Bauer C, Duewell P, Mayer C, Lehr HA, Fitzgerald KA, Dauer M, et al. Colitis induced in mice with dextran sulfate sodium (DSS) is mediated by the NLRP3 inflammasome. *Gut* 2010;**59**:1192−9.
53. Tourkochristou E, Aggeletopoulou I, Konstantakis C, Triantos C. Role of NLRP3 inflammasome in inflammatory bowel diseases. *World J Gastroenterol* 2019;**25**:4796−804.
54. Mei Y, Fang C, Ding S, Liu X, Hu J, Xu J, et al. PAP-1 ameliorates DSS-induced colitis with involvement of NLRP3 inflammasome pathway. *Int Immunopharmacol* 2019;**75**:105776.
55. Perera AP, Fernando R, Shinde T, Gundamaraju R, Southam B, Sohal SS, et al. MCC950, a specific small molecule inhibitor of NLRP3 inflammasome attenuates colonic inflammation in spontaneous colitis mice. *Sci Rep* 2018;**8**:8618.
56. Xu X, Li J, Long X, Tao S, Yu X, Ruan X, et al. C646 protects against DSS-induced colitis model by targeting NLRP3 inflammasome. *Front Pharmacol* 2021;**12**:707610.
57. Gong Z, Zhao S, Zhou J, Yan J, Wang L, Du X, et al. Curcumin alleviates DSS-induced colitis *via* inhibiting NLRP3 inflammsome activation and IL-1β production. *Mol Immunol* 2018;**104**:11−9.